The Astrophysical Journal, 885:62 (16pp), 2019 November 1 https://doi.org/10.3847/1538-4357/ab4282

Broadband X-Ray Constraints on the Accreting Black Hole in Quasar 4C 74.26

P. Tzanavaris[1,2], T. Yaqoob[1,2,3], S. LaMassa[4], M. Yukita[2,3], and A. Ptak[2,3]
[1] University of Maryland, Baltimore County, 1000 Hilltop Circle, Baltimore, MD 21250, USA
[2] Laboratory for X-ray Astrophysics, NASA/Goddard Spaceflight Center, Mail Code 662, Greenbelt, MD 20771, USA
[3] Department of Physics and Astronomy, The Johns Hopkins University, Baltimore, MD 21218, USA
[4] Space Telescope Science Institute, 3700 San Martin Drive, Baltimore, MD 21218, USA
Received 2019 January 31; revised 2019 August 19; accepted 2019 September 5; published 2019 October 31

Abstract

X-ray data for quasar 4C 74.26 have previously been modeled with a broad Fe Kα emission line and reflection continuum originating in the inner part of the accretion disk around the central supermassive black hole (SMBH), i.e., the strong-gravity regime. We modeled broadband X-ray spectra from *Suzaku* and *NuSTAR* with MYTORUS, self-consistently accounting for Fe Kα line emission, as well as direct and reflected continuum emission, from matter with a finite column density. A narrow Fe Kα emission line originating in an X-ray reprocessor with solar Fe abundance far from the central SMBH is sufficient to produce excellent fits for all spectra. For the first time, we are able to measure the global column density, out of the line of sight, to be in the range $\sim$1.5 to $\sim 2.9 \times 10^{24}$ cm^{-2}, i.e., in the Compton-thick regime, while the line-of-sight column density is Compton-thin in all observations. The Fe Kα emission line is unresolved in all observations but one. The Compton-scattered continuum from distant matter removes the need for relativistic broadening of the Fe Kα emission line, which is required for SMBH spin measurements. The resolved line observation can alternatively be modeled with a relativistic model but we do not find evidence for a truncated accretion disk model. We conclude that the X-ray emission in these 4C 74.26 data is unlikely to originate in the inner accretion disk region and thus cannot be used to measure SMBH spin.

Key words: black hole physics – galaxies: active – galaxies: individual (4C 74.26) – radiation mechanisms: general – scattering

1. Introduction

All galaxies with bulges are thought to harbor supermassive black holes (SMBHs, $\sim 10^6$–$10^9\,M_\odot$) in their centers (see Graham 2016 for a review). The resulting strong gravity in the nuclear region leads to gravitational collapse of surrounding material via disk accretion onto the nuclear SMBH, releasing large amounts of energy. In turn, a population of energetic, hot electrons, likely residing in a diffuse, hot corona, are thought to induce thermal inverse Compton upscattering of optical/UV photons from the accretion disk, producing a primary X-ray power-law continuum, which is one of the key signatures of active galactic nuclei (AGNs). This continuum may then irradiate the accretion disk, or gaseous structures such as clumpy clouds or a torus that are more distant from the central SMBH. The interaction of the primary X-ray continuum with optically thick, cold, neutral and/or mildly ionized material can give rise to a series of fluorescent emission lines, and associated Compton-scattered, or "reflected," continua. Due to a combination of cosmic abundance and fluorescent yield, most prominent is the Fe Kα emission line at 6.4 keV ($\sim$1.94 Å) and its associated reflection continuum (George & Fabian 1991).

According to the "AGN unification scheme" (Antonucci 1993; Urry & Padovani 1995), galaxies with accreting SMBHs (i.e., AGNs) are broadly classified as Type 1 or 2. The distinction is based on viewing angle, so that Type 1 are viewed face-on and Type 2 edge-on; intermediate types are also possible. As a result, Type 1 are more likely to afford a direct view of the strong-gravity region because their line of sight to the central engine is less likely to be obscured.

The Fe Kα emission line comes in two types, often referred to simply as *narrow* and *broad* line. The "narrow core" component of the line (FWHM $\lesssim 2000\,\mathrm{km\,s^{-1}}$) is detected in the great majority of both Type 1 and Type 2 AGNs with luminosities $L_{\mathrm{X,2.0–10.0\,keV}} < 10^{45}$ erg s^{-1} (Yaqoob & Padmanabhan 2004; Nandra 2006; Shu et al. 2010, 2011; Fukazawa et al. 2011; Ricci et al. 2014). An additional, relativistically broadened component (FWHM several thousands to tens of thousands km s^{-1}) is thought to be widespread and found in *at least* $\sim$36% of AGNs (de la Calle Pérez et al. 2010; see also, e.g., Porquet et al. 2004; Jiménez-Bailón et al. 2005; Guainazzi et al. 2006; Nandra et al. 2007; Brenneman & Reynolds 2009; Patrick et al. 2012; Liu et al. 2015; Mantovani et al. 2016; Baronchelli et al. 2018).

The smaller FWHM of the narrow line suggests that the reprocessing of the X-ray continuum is occurring in distant matter at hundreds to thousands of gravitational radii from the SMBH and its immediate environment. Measurement of the properties of the narrow line and its associated reflection continuum then provides unique constraints on the physical properties of the larger-scale structure associated with the central engine. In contrast, the broad line should have its origin closer to the SMBH, implying that reprocessing of the intrinsic X-ray continuum is taking place at the accretion disk itself. In this case the width of the line is a combination of Doppler and general relativistic effects, which lead to line broadening or "blurring," with the contributions becoming progressively stronger as one approaches, and up to, the innermost stable circular orbit (ISCO), the closest limit to the black hole where the disk remains geometrically thin, optically thick, and radiatively efficient (for reviews see Fabian et al. 1989; Reynolds & Nowak 2003; Miller 2007; Reynolds 2016). Because the ISCO location depends directly on black hole spin, the latter affects the profile of the observed relativistically broadened line. In practice, the effect of black hole spin on the

line profile is not definitive, because it is degenerate with the unknown radial line emissivity profile and Fe abundance. Moreover, the effects of black hole spin manifest themselves at the extreme energy limits of the line profile, i.e., regimes that are most sensitive to correct deconvolution of the underlying continuum (which must be deduced from spectral fitting simultaneously with the line profile). Nevertheless, these effects have been modeled in detail, forming the basis of the X-ray reflection method of spin determination. As a result, there are a large number of black hole spin measurements in the literature for both X-ray binaries (Middleton 2016 and references therein) and AGNs (Brenneman 2013, and references therein). Constraining black hole spin represents one of the holy grails of astrophysical science, with far-reaching implications for our understanding of black holes and their impact on their surrounding environment. It is an essential step in any Kerr-metric-based test of strong-field general relativity. In addition it can provide insight into the mechanism driving nuclear jets, such as the paradigm of Blandford & Znajek (1977) of rotational energy extraction from a central Kerr (i.e., rotating) black hole, which directly affects galaxy environment and by extension galaxy evolution.

However, the results for spin measurements via the reflection method to date span the allowed spin values, even for the same object and data. At the same time, best-fitting results for some of the most well known broad-line AGNs often require highly supersolar Fe abundances, such as up to $\sim$4$\times$ solar for MCG 6-30-15 (e.g., Chiang & Fabian 2011), $\sim$4.6 or $\sim$4$\times$ solar for NCG 3783 (Brenneman et al. 2011; Reynolds et al. 2012), or even $>$8.4$\times$ solar for Fairall 9 (Lohfink et al. 2012). Patrick et al. (2012) noted the degeneracy between spin and Fe abundance, with high spin magnitudes requiring supersolar abundances. In addition, it has now been shown that some AGNs previously well-known for harboring a broad Fe Kα emission line can be modeled exclusively with a narrow line from distant matter and the reflection continuum associated with it, using only solar Fe abundance (e.g., Yaqoob et al. 2016 for Fairall 9; Murphy & Nowak 2014 for MCG +8−11−11). In such cases, since a broad Fe Kα emission line is not required in the model, black hole spin determination from the X-ray spectrum is not possible.

The quasar 4C 74.26 is one of the nearest ($z = 0.104$) powerful broad-line radio galaxies of class FRII (Riley et al. 1989). Woo & Urry (2002) measured a bolometric luminosity $L_{\rm bol} \sim 2 \times 10^{46}$ erg s^{-1} and estimated a black hole mass $\sim 4 \times 10^9$ $M_\odot$. In the optical, permitted lines have been reported ($\sim$8000–11,000 km s^{-1}, Riley et al. 1989; Corbin 1997; Brinkmann et al. 1998; Robinson et al. 1999) that are very broad, as far as optical lines are concerned.

In 4C 74.26 most previous works on the X-ray spectrum, using a variety of telescopes, instruments, and models, reported a strong, broad Fe Kα line with a width equivalent to a Gaussian σ of up to $\sim$600 eV, corresponding to a velocity FWHM of $\sim$0.22c, where c is the speed of light. An equivalent width (EW) of up to $\sim$300 eV was reported for the broad Fe Kα line, a value that is not atypical of broad Fe Kα lines reported in other AGNs. Only sometimes was an accompanying narrow component also reported. The earliest modeling results with the *Advanced Satellite for Cosmology and Astrophysics* (*ASCA*) included either a narrow line only (Brinkmann et al. 1998) or a broad line only (Sambruna et al. 1999; Hasenkopf et al. 2002). Hasenkopf et al. (2002) reported only a broad line for the same *ASCA* data, and also for *BeppoSAX* data. In more recent work, a broad line was reported by Ballantyne & Fabian (2005), Ballantyne (2005), Larsson et al. (2008), Patrick et al. (2012), Tombesi et al. (2014), Gofford et al. (2013), Di Gesu & Costantini (2016), Lohfink et al. (2017), and Bhatta et al. (2018). In contrast, Noda et al. (2013) reported a narrow line only. Among these results supersolar abundances were reported by Larsson et al. (2008, up to 4.8$\times$ solar), while Gofford et al. (2013) reported Fe *under* abundances of $\sim$0.3$\times$ solar. Patrick et al. (2012) and Gofford et al. (2013) also reported fitting a narrow-line component. Further, four works estimated or assumed SMBH spin values for this, and Bhatta et al. (2018) assumed a maximally spinning black hole (spin value of 1), Lohfink et al. (2017) reported constraining spin values to $>$0.5. Further details on previous work are given in the Appendix.

4C 74.26 is an excellent test case for broad Fe Kα line modeling. Among AGNs for which a broad line has been claimed to be prominent, it has a high luminosity and low redshift, thus occupying a region of parameter space that has not been thoroughly investigated. In addition, its X-ray spectrum is not particularly complicated, representing a relatively straightforward case for X-ray spectral modeling.

Note that studies of AGNs have generally only measured the line-of-sight equivalent hydrogen column density (labeled $N_{\rm H,Z}$ in this paper, Section 3.2). However, a model such as MYTORUS (Murphy & Yaqoob 2009; Yaqoob 2012) can measure the line-of-sight column density as well as the *global* column density, out of the line of sight (labeled $N_{\rm H,S}$ in this paper, Section 3.2). This is crucial because a key ingredient for population synthesis modeling of the cosmic X-ray background (CXB) spectrum is the number density of "Compton-thick" (highly obscured, equivalent hydrogen column density $\gtrsim 10^{24}$ cm^{-2}) versus "Compton-thin" AGNs. However, traditional analyses that use the "Compton-thick fraction" as a parameter do not distinguish between sources that are Compton-thick *only* in the line of sight and those that are *globally* Compton-thick; yet such a distinction affects the observed X-ray spectrum. Measuring the separate column densities is then critical, because one of them may be Compton-thick and the other Compton-thin (LaMassa et al. 2014; Yaqoob et al. 2015).

In this paper we test the hypothesis that the *Suzaku* and *NuSTAR* spectra of 4C 74.26 can be fitted only with a narrow Fe Kα line emission component and associated reflected continuum. The implication of this would be that, since the narrow Fe Kα emission line does not originate in the strong-gravity regime, it would not be possible to measure black hole spin. We use MYTORUS, which self-consistently models the Fe Kα line emission doublet together with its associated reflection continuum and solar Fe abundance. Unlike previous work, this also allows us to constrain the equivalent hydrogen column density both into and out of the line of sight independently. MYTORUS models the Compton reflection continuum from matter with a finite column density, which can masquerade as a broad component of the Fe Kα line, and more so than the usual reflection from disk models with infinite column density.

The structure of the paper is as follows. In Section 2 we describe the observations and data reduction. Spectral modeling methodology is discussed in Section 3. Results are presented and discussed in Section 4. Finally, a summary and conclusions are presented in Section 5. We use a concordance cosmology, namely $H_0 = 70$ km s^{-1} Mpc^{-1}, $\Omega_\Lambda = 0.73$, $\Omega_M = 0.27$ throughout.

Table 1
Exposure Times and Count Rates for *Suzaku* and *NuSTAR* Spectra

Telescope	ObsID	Date/Time	Detector	Exposure (ks)	Energy ranges (keV)	Count Rate (count s^{-1})	Percentage of On-source Rate	References
(1)	(2)	(3)	(4)	(5)	(6)	(7)	(8)	(9)
Suzaku	**702**057010	2007 Oct 28T10:21:17	XIS	91.6	1.0–1.5, 2.3–9.5	1.0230 ± 0.0020	98.3	(1), (2), (3), (4), (5)
			PIN	87.3	12.0–35.0	0.1115 ± 0.0025	22.0	
Suzaku	**706**028010	2011 Nov 23T12:58:54	XIS	101.4	1.0–1.5, 2.3–10.0	0.9601 ± 0.0018	98.2	(2)
			PIN	109.7	18.0–39.0	0.0528 ± 0.0015	23.6	
NuSTAR	6000108000**2**	2014 Sep 21T15:21:07	FPMA	19.1	3–43	0.7658 ± 0.0065	95.6	(6)
			FPMB			0.7290 ± 0.0063	95.6	
NuSTAR	6000108000**4**	2014 Sep 22T11:51:07	FPMA	56.6	3–43	0.8022 ± 0.0039	95.7	(6)
			FPMB			0.7652 ± 0.0038	95.7	
NuSTAR	6000108000**6**	2014 Oct 30T23:06:07	FPMA	90.9	3–43	0.7035 ± 0.0028	95.3	(6)
			FPMB			0.6833 ± 0.0028	95.4	
NuSTAR	6000108000**8**	2014-12-22T06:16:07	FPMA	42.8	3–43	0.7171 ± 0.0042	95.5	(6)
			FPMB			0.6916 ± 0.0041	95.5	
NuSTAR	total		FPMA	209.4	3–43	0.7133 ± 0.0018	99.6	(6)
			FPMB			0.6882 ± 0.0018	99.6	

Note. Column (3) is the observation start-date (header keyword DATE-OBS). Column (5) is the exposure time (header keyword EXPOSURE). Column (7) is the background-subtracted count rate in the energy bands specified. For the XIS, this is the rate per XIS unit, averaged over XIS0, XIS1, and XIS3. Column (8) is the background-subtracted source count rate as a percentage of the total on-source count rate, in the energy intervals shown.
References. (1) Larsson et al. (2008), (2) Tombesi et al. (2014), (3) Patrick et al. (2012), (4) Gofford et al. (2013), (5) Noda et al. (2013), (6) Lohfink et al. (2017).

2. Observations and Data Reduction

In this paper we use two *Suzaku* and four *NuSTAR* archival observations. Details of the observations are given in Table 1, including references from the literature that report results of previous analyses of these observations. As can be seen from column 6, both *Suzaku* and *NuSTAR* have broadband X-ray coverage, which is critical for modeling the reflection continuum well.

2.1. Suzaku

We study two archival observations of 4C 74.26 carried out by the joint Japan/US X-ray astronomy satellite, *Suzaku* (Mitsuda et al. 2007). For brevity, we refer to the *Suzaku* ObsIDs as 702 and 706.

Suzaku had four X-ray imaging spectrometers (XIS, Koyama et al. 2007) and a collimated hard x-ray detector (HXD, Takahashi et al. 2007). Each XIS consisted of four CCD detectors with a field of view of 17.8 × 17.8 $arcmin^2$. Of the three front-side-illuminated (FI) CCDs (XIS0, XIS2, and XIS3), XIS2 had ceased to operate prior to the observations studied here. We thus used FI CCDs XIS0 and XIS3, as well as the back-side-illuminated (BI) XIS1. The operational bandpass is (0.2–12) 0.4–12 keV for (BI) FI. However, the useful bandpass depends on the signal-to-noise ratio of the background-subtracted source data since the effective area strongly diminishes at the ends of the operational bandpass. The HXD consisted of two non-imaging instruments (the PIN and GSO) with a combined bandpass of ∼10–600 keV. Both instruments are background-limited, with the GSO having the smaller effective area. We only used the PIN data because the GSO data did not provide a reliable spectrum. ObsID 702 was acquired at the "HXD-nominal," and 706 at the "XIS-nominal" position.

The principal data selection and screening criteria for the XIS were the selection of only ASCA grades 0, 2, 3, 4, and 6, the removal of flickering pixels with the FTOOL `cleansis`, and exclusion of data taken during satellite passages through the South Atlantic Anomaly (SAA), as well as for time intervals less than 256 s after passages through the SAA, using the T_SAA_HXD house-keeping parameter. Data were also rejected for Earth elevation angles (ELV) less than 5°, Earth daytime elevation angles (DYE_ELV) less than 20°, and values of the magnetic cutoff rigidity less than 6 GeV/c^2. Residual uncertainties in the XIS energy scale are of the order of 0.2% or less (or ∼13 eV at 6.4 keV). The cleaning and data selection resulted in the net exposure times shown in Table 1.

We extracted XIS source spectra in a circular extraction region with a radius of 3′.5. We constructed background XIS spectra from off-source areas of the detector, after removing a circular region with a radius of 4′.5 centered on the source, as well as the calibration sources (using rectangular masks). The background-subtraction method for the HXD/PIN used the files `ae702057010_hxd_pinbgd.evt`, `ae706028010_hxd_pinbgd.evt`, corresponding to the "tuned" version of the background model.

Spectral response matrix files (RMFs) and telescope effective area files (ARFs) for the XIS data were made using the mission-specific FTOOLS XISRMFGEN and XISSIMARFGEN, respectively. The XIS spectra from XIS0, XIS1, and XIS3 were combined into a single spectrum for spectral fitting. The three RMFs and ARFs were all combined, using the appropriate weighting (according to the count rates and exposure times for each XIS), into a single response file for the combined XIS background-subtracted spectrum. For the HXD/PIN spectrum, the supplied spectral response matrices appropriate for the times and nominal pointing mode of the observations (`ae_hxd_pinhxnome4_20080129.rsp` for 702 and `ae_hxd_pinxinome11_20110601.rsp` for 706) were used for spectral fitting.

We determined useful energy bandpasses for the spectrum from each instrument by first assessing background-subtraction systematics. For XIS we used spectra with a uniform binning, with 30 eV bin width, and found that in the 0.3–9.5 keV and 0.3–10.0 keV bands, for observations 702 and 706 respectively, there were >20 counts per bin for the unscaled background, total source, and background-subtracted source. In addition, in

these regions, the background counts, scaled by the relative areas of source versus background region, were <50% of the background-subtracted source counts. Since the counts per bin were >20 in the stated energy bands, we were able to use the χ^2 statistic for spectral fitting. Note that we did not group spectral bins using a signal-to-noise ratio threshold, which can wash out weak features. We further excluded spectral regions that are subject to calibration uncertainties in the effective area due to atomic features. Specifically, it is known that this calibration is poor in the ranges ∼1.8–1.9 and ∼2.0–2.4 keV due to Si in the detector and Au M edges in the telescope, respectively. The effective area also has a steep change at ∼1.56 keV due to Al in the telescope. Thus for the purposes of spectral fitting we conservatively chose to exclude the energy range 1.5–2.3 keV. We also excluded the region below 1 keV, because this suggested the need for an extra local continuum component and does not affect our higher energy results. For HXD/PIN, we first performed background subtraction on the original 256-bin spectrum to identify the maximum continuous spectral range with nonnegative background-subtracted counts, since negative background-subtracted counts would indicate an obvious breakdown of the background model. This was then rebinned uniformly to bin widths of 1.5 keV, leading to the final useful spectral ranges 12.0–35.0 and 18.0–39.0 keV for observations 702 and 706, respectively.

The relative cross-normalization of the XIS/PIN data involves many factors (see Yaqoob 2012 for a detailed discussion). Observation 702 has "HXD-nominal," while 706 has "XIS-nominal" pointing. The recommended PIN:XIS ratios (hereafter $C_{\rm PIN:XIS}$) are then 1.18 and 1.16, respectively.[5] These values do not take into account background-subtraction systematics, sensitivity to spectral shape, and other factors that could affect the actual ratio. Allowing $C_{\rm PIN:XIS}$ to be a free parameter does not optimally address this issue, because that could skew the best-fitting model parameters at the expense of obtaining a $C_{\rm PIN:XIS}$ "best-fit" value, which in actuality is unrelated to the true normalization ratio of the instruments. We thus carried out preliminary investigations for each data set (Section 3) before deciding whether we could fix $C_{\rm PIN:XIS}$. For comparison, we also performed XIS-only spectral fits.

2.2. NuSTAR

We studied four archival observations carried out by the *NuSTAR* mission (Harrison et al. 2013). We reduced the observations to obtain calibrated and screened level 2 event lists from the level 1 data by means of the standard *NuSTAR* pipeline NUPIPELINE,[6] which is part of the HEASOFT 6.24 software package.

We used the NUPRODUCTS pipeline to extract source and background spectra and corresponding responses for each of the two detectors, focal plane modules A and B (FPMA, FPMB). We chose circular source regions centered on the source with 60″ radii. For background we chose rectangular regions covering essentially the full area of the CCD, except for the source region. Initial examination of the individual spectra showed that there were too few counts to allow reliable fitting over a substantial spectral range. We thus combined all spectra and produced a master source and background spectrum for each detector. We checked that there was minimal variability in normalization or spectral shape between observations, so that this process did not wash out any significant spectral features that might be unique to a single observation.

We applied binning factors of 3 to the master source spectrum between 23.6 and 30 keV, and 8 above 30 keV. This was the minimal binning scenario that ensured a minimum of 20 counts per channel for the unscaled background, as well as both raw and background-subtracted source counts up to 43 keV for both FPMA and FPMB. In the same energy range this choice led to a scaled background as a fraction of the background-subtracted source counts that was $\lesssim$50% per channel. Since *NuSTAR* data are not well calibrated below 3 keV, this binning allowed the use of χ^2 statistics in the energy range 3–43 keV. We fitted the FPMA and FPMB spectra simultaneously, allowing the cross-normalization to be free (see Section 3.9).

3. Spectral Modeling: Fe Kα Line Emission and Reflection Continuum

3.1. Overview

Our primary goal was to apply a physical, self-consistent model for the Fe Kα line and its associated reflected continuum that does not assume the presence of a relativistically broadened line, and thus to determine whether the 4C 74.26 spectral data can be modeled without strong-gravity relativistic effects that arise close to the central black hole at gravitational radii $r_g \lesssim 100$. There are widespread claims in the literature that the Fe Kα line emission in these data is broadened due to such effects, thus allowing measurements of black hole spin. In addition, Fe abundances in previous work range from subsolar to highly supersolar (see Section 1). Instead, we tested specifically whether these data can be fitted exclusively with narrow Fe Kα line emission and an associated reflection continuum from distant matter with a finite column density, with line and reflection continuum calculated self-consistently, and solar Fe abundance only. For this purpose, we applied the toroidal X-ray reprocessor model MYTORUS (Murphy & Yaqoob 2009; Yaqoob 2012). We stress that the line and associated reflection continuum are coupled by the atomic physics and are produced in tandem by the model, thus preserving self-consistency between the line and Compton-scattered continuum. Other models that self-consistently produce the line and reflection continuum exist but were not used in this study. The model of Ikeda et al. (2009) is not publicly available, the TORUS of Brightman & Nandra (2011) has some errors (see Liu & Li 2014; Baloković et al. 2018, for details), while CTORUS (Liu & Li 2014) is too restrictive for our purposes. BORUS (Baloković et al. 2018) came online after the bulk of this work was complete. We note, though, that Baloković et al. (2018) reported mostly good agreement with MYTORUS (see their Appendix).

We used XSPEC (Arnaud 1996, version 12.10.0*c*) and the χ^2 statistic for minimization. We included absorption from material between the observer and the source ($N_{\rm H}^{\rm inter}$), modeled with a `phabs` component and fixed at the tabulated Galactic column density value of $1.16 \times 10^{21}\,{\rm cm}^{-2}$ (Kalberla et al. 2005), unless stated otherwise. We used photoelectric cross sections from Verner et al. (1996) with element abundances from Anders & Grevesse (1989).

For each parameter we calculated statistical errors for 90% confidence (one parameter of interest, corresponding to

[5] ftp://legacy.gsfc.nasa.gov/suzaku/doc/xrt/suzakumemo-2008-06.pdf
[6] http://heasarc.gsfc.nasa.gov/docs/nustar/analysis/nustar_swguide.pdf

$\Delta\chi^2 = 2.706$), by iteratively stepping away from the best-fit minimum. Errors for line flux and equivalent width were determined as explained in Section 3.5. We do not give statistical errors on continuum fluxes and luminosities because absolute continuum fluxes are dominated by systematic uncertainties that are not well quantified, typically of the order of ~10%–20% (e.g., Tsujimoto et al. 2011; Madsen et al. 2017).

3.2. MYTORUS Model

We provide here a brief overview of salient characteristics of the model. For in-depth descriptions see Murphy & Yaqoob (2009), Yaqoob & Murphy (2011), Yaqoob (2012), LaMassa et al. (2014), Yaqoob et al. (2016), and the MYTORUS manual.[7] The baseline geometry consists of a neutral-matter torus of circular cross section, with diameter characterized by the equatorial equivalent hydrogen column density. A central, isotropic X-ray source illuminates the torus, and the global covering factor of the reprocessor is 0.5, corresponding to a half-opening angle of 60°. Note that the model can also be used to mimic other geometrical configurations (Yaqoob 2012, Figure 15) so that one is not limited to modeling a strictly toroidal geometry. Thus in spite of the nomenclature used for the MYTORUS model and its components, it is in fact a more general analysis tool for reprocessing of primary X-ray continua. The model self-consistently produces the Fe Kα and Fe Kβ fluorescent emission-line spectrum, as well as absorption and Compton scattering effects on continuum and line emission. At present, abundances are fixed at solar values. Free relative normalizations between different components can be used to accommodate a variety of different actual geometries compared to the specific assumptions in the original calculations, as well as time delays between the various model continua and line photons. This, however, does not break the self-consistency between fluorescent line emission and reflection continuum.

The model's direct, line-of-sight ("zeroth," Z) observed continuum component is obtained from the intrinsic continuum via a multiplicative table model (`mytorus_Ezero_v00.fits` in XSPEC) and is not affected by the global geometry. If the angle between the symmetry axis of the torus and the observer's line of sight ($\theta_{\rm obs}$) is greater than the torus opening angle, this continuum is diminished via absorption and removal of photons from the line of sight by Compton scattering. Further, the global distribution of matter gives rise to a Compton-scattered ("reflected," S) continuum and fluorescent line (L) emission. The reflected continuum is implemented as an additive table model (`mytorus_scatteredH500_v00.fits`); this corresponds to a power-law incident continuum with termination energy of 500 keV and photon index $1.4 < \Gamma < 2.6$. The Fe Kα and Fe Kβ emission lines are implemented with another additive table model (`mytl_V000010nEp000H500_v00.fits`). Each table has separate parameters for incident power-law continuum normalization, photon index Γ, angle $\theta_{\rm obs}$, redshift z, and equivalent hydrogen column density.[8] In general, corresponding parameters among tables are tied to each other, unless stated otherwise. In particular, the hydrogen equivalent column density associated with the reflection continuum is always identical, and tied to, the one for the fluorescent emission line component since both this continuum and these emission lines are the result of Compton scattering due to the global matter distribution. Thus, we denote this column density with the single symbol, $N_{\rm H,S}$.

As 4C 74.26 is a Type 1 AGN, we assume a face-on geometry ($\theta_{\rm obs} = 0°$) and decouple $N_{\rm H,S}$ from $N_{\rm H,Z}$, so that $N_{\rm H,S}$ represents the global column density, out of the line-of-sight, while $N_{\rm H,Z}$ models the line-of-sight column density, which may have a different value. The reflection spectrum and fluorescent line emission for inclination angles that do not intercept the torus are similar to those for the face-on case, and the differences are too small for the data to be sensitive to them. An illustrative sketch of the assumed configuration is shown in Figure 1. Table 2 summarizes the main continua, associated column densities, terminology, and symbols used. For a more detailed discussion see Yaqoob (2012), Section 4.5.2.

We also include a parameter A_S for the relative normalization between the direct and scattered continuum, which is 1.0 for the baseline geometry, implying either a constant intrinsic X-ray continuum flux or a variable one for which the X-ray reprocessor is compact enough that the Compton-scattered flux responds to the intrinsic continuum on timescales much less than the integration time. Values $A_s \neq 1.0$ imply departures of the covering factor from 0.5, time delays between intrinsic and scattered continua, or both. However, the relationship of A_S to the covering factor is not simple because the detailed shape of the scattered continuum varies with the covering factor. Similarly, A_L is the relative normalization of the Fe Kα line emission, with $A_L = 1$ having a similar meaning to $A_S = 1$; we set $A_L = A_S$ throughout because otherwise the model's self-consistency is broken. Both parameters are implemented by XSPEC `constant` components that multiply the S and L tables.

3.3. Fe Kα Line Energy

In MYTORUS, the Fe Kα line is modeled as a Kα_1, Kα_2 doublet at 6.404 and 6.391 keV with a branching ratio of 2:1, giving a weighted mean centroid energy of $E_{\rm rest} = 6.400$ keV. The Fe Kβ line is centered at 7.058 keV. In *Suzaku* or *NuSTAR* data the line peaks are likely to be offset due to instrumental calibration systematics and/or mild ionization effects. We thus used the best-fit model redshift parameter to calculate an effective Fe Kα line energy offset in the observed frame, so that positive shifts imply Fe Kα centroid energies higher than $E_{\rm rest}$.

3.4. Fe Kα Line Velocity Width

We implemented line velocity broadening via a Gaussian convolution kernel (`gsmooth` in XSPEC) with energy width $\sigma_E = \sigma_L \left(\frac{E_0}{6\ {\rm keV}}\right)^{\alpha}$, where E_0 is the centroid energy, and σ_L and α are free parameters; we set $\alpha = 1$ for a velocity width that is independent of energy. In velocity units one obtains ${\rm FWHM} = 2.354\, c\frac{\sigma_L}{6}$, or $117{,}700\sigma_L$ (keV) km s^{-1}. Although the reflection continuum includes edges, we did not apply velocity broadening on it, because this significantly slows down the fitting process and previous work has shown that the effect is minimal. Even so, we tested the effect of including broadening using `gsmooth` in XSPEC for our data. At most this induces a fractional change in parameter values of $\lesssim$3%, the only exception being $N_{\rm H,S}$ for ObsID 706. In this case the

[7] http://mytorus.com/manual

[8] For brevity, we later refer to the Z, S, and L tables as `etable_mytorusZ`, `atable_mytorusS`, `atable_mytorusL`.

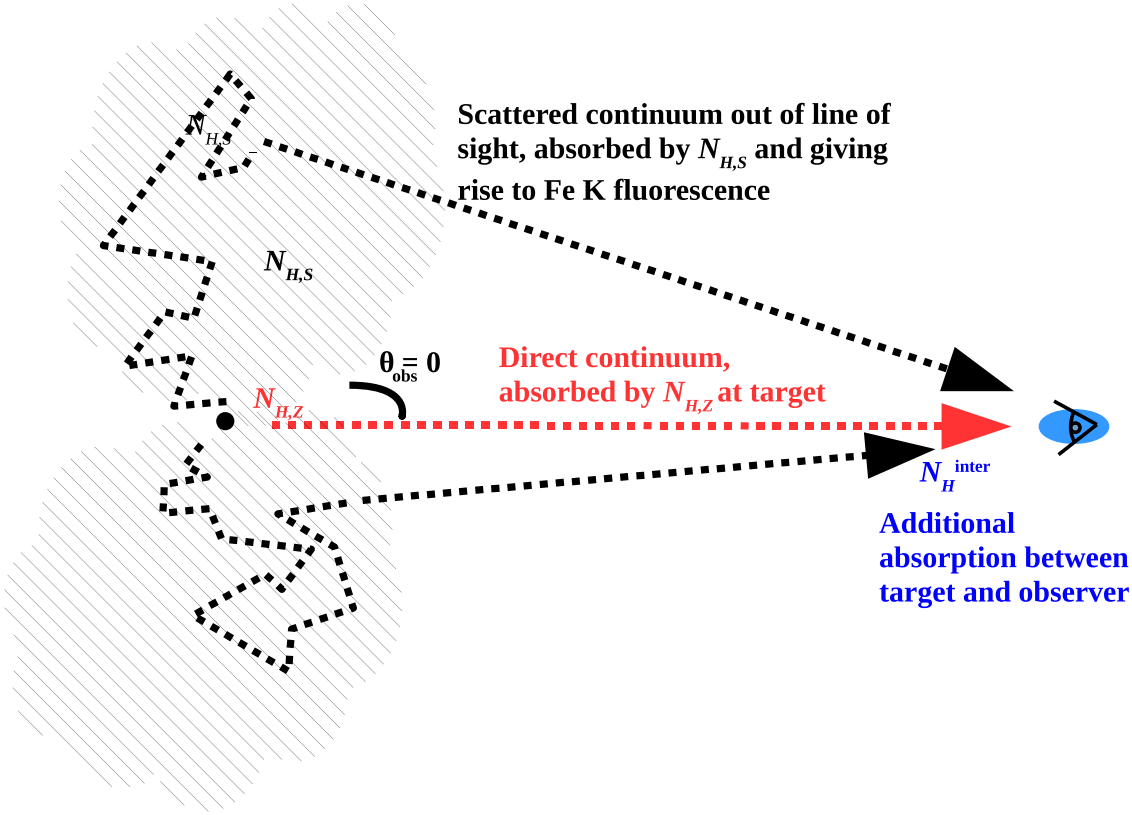

Figure 1. Illustration of the geometry assumed in this paper (see also Table 2). Part of the intrinsic continuum experiences no Compton scattering and reaches the observer along the line of sight, in the process being attenuated by an equivalent hydrogen column density $N_{\rm H,Z}$ ("direct" or "zeroth" or line-of-sight continuum). Another part of the intrinsic continuum experiences Compton scattering out of the line of sight, and is absorbed by a column density $N_{\rm H,S}$, which also gives rise to the Fe Kα and Kβ fluorescent line emission. Since $N_{\rm H,S}$ is associated with any location out of the line of sight, it is a "global" property. A cross section of the putative torus is drawn in the plane of the paper and is for illustration only. In reality X-ray reprocessing may occur in a collection of clouds or clumps.

Table 2
Summary of Continua, Associated Equivalent Hydrogen Column Densities, and Related Terminologies in This Paper

Continuum Type (1)	MYTORUS Symbol (2)	Associated Equivalent Hydrogen Column Density (3)	MYTORUS XSPEC Table (4)
Direct ("zeroth")	Z	$N_{\rm H,Z}$ (line of sight)	`mytorus_Ezero_v00.fits`
Compton-scattered ("reflected")	S	$N_{\rm H,S}$ ("global")	`mytorus_scatteredH500_v00.fits`

Note. $N_{\rm H,S}$ is also the column density associated with Fe Kα and Kβ fluorescent line emission. The direct continuum is only attenuated along the line of sight by the associated column density $N_{\rm H,Z}$ and is not affected by Compton scattering. In contrast, the reflected continuum is Compton-scattered out of the line of sight by the associated column density $N_{\rm H,S}$. A column density $N_{\rm H}^{\rm inter}$ due to matter between the observer and the source further attenuates the total continuum that reaches the observer. See also Figure 1.

fractional change is ∼20%, but this is more than 3–9 times smaller than the statistical fractional error of 65%–186% (Section 4.4).

3.5. Fe Kα Line Flux and Equivalent Width

After the best fit was obtained, we isolated the emission-line table `atable_mytorusL` to measure the observed flux of the Fe Kα line, $I_{\rm FeK\alpha}$, in an energy range excluding the Fe Kβ line with the XSPEC `flux` command. We measured the equivalent width (EW) by means of the line flux and the total monochromatic continuum flux at the observed line peak energy. $I_{\rm FeK\alpha}$ and EW in the AGN frame were then obtained by multiplying observed values by $(1 + z)$. As these are not explicit model parameters, we estimated fractional errors by using the fractional errors on A_S.

3.6. Continuum Fluxes and Luminosities

We calculated continuum fluxes and luminosities using the best-fit model and the `flux` and `lumin` commands in XSPEC. We obtained absorbed fluxes in the observed frame (labeled "obs") and both absorbed and unabsorbed luminosities in the AGN frame ("rest, abso," "rest, unabso," respectively). In the latter case a redshift value of 0.104 was input to `lumin`. For absorbed values, we used the total best-fit model minus any additional Gaussian emission lines, and for unabsorbed ones

Table 3
Spectral Fitting Results for *NuSTAR* and *Suzaku* Observations of 4C 74.26 Obtained from Fitting with the MYTORUS Model

(1)	(2)	(3)	(4)	(5)	(6)	(7)
1	Mission/ObsID	*NuSTAR*	*Suzaku*-702	*Suzaku*-702	*Suzaku*-706	*Suzaku*-706
2	Instruments	FPMA/B	XIS	XIS, PIN	XIS	XIS, PIN
3	χ^2/d.o.f.	1377.1/1211	295.5/255	321.6/269	301.4/261	310.8/273
4	χ^2_ν	1.137	1.159	1.195	1.155	1.138
5	$P_{\rm null}$	0.001	0.041	0.015	0.043	0.058
6	$\theta_{\rm obs}$ (deg)	0 (f)	0 (f)	0 (f)	0 (f)	0 (f)
7	$C_{\rm cross}$	$1.03^{+0.01}_{-0.01}$	...	1.18 (f)	...	$1.80^{+0.30}_{-0.40}$
8	$N_{\rm H}^{\rm inter}$	0.116 (f)	0.116 (f)	0.116 (f)	$0.268^{+0.019}_{-0.019}$	$0.268^{+0.019}_{-0.018}$
9	$N_{\rm H,Z}$ (10^{22} cm^{-2})	$1.224^{+0.321}_{-0.344}$	$0.192^{+0.016}_{-0.015}$	$0.189^{+0.015}_{-0.015}$	$14.549^{+3.125}_{-2.613}$	$14.431^{+3.119}_{-2.562}$
10	$N_{\rm H,S}$ (10^{22} cm^{-2})	$289.960^{+52.310}_{-45.530}$	$40.262^{+114.648}_{-23.150}$	$288.760^{+124.750}_{-85.710}$	>53.478	$149.060^{+278.200}_{-97.392}$
11	A_Z	...	...	...	$0.325^{+0.077}_{-0.087}$	$0.320^{+0.085}_{-0.083}$
12	A_S	$0.716^{+0.087}_{-0.083}$	$0.679^{+0.535}_{-0.203}$	$0.702^{+0.118}_{-0.114}$	$1.483^{+1.155}_{-0.349}$	$1.404^{+0.614}_{-0.310}$
13	Γ	$1.919^{+0.019}_{-0.020}$	$1.921^{+0.015}_{-0.015}$	$1.914^{+0.014}_{-0.015}$	$2.012^{+0.038}_{-0.040}$	$2.012^{+0.039}_{-0.040}$
14	$E_{\rm shift}$ (eV)	$0.7^{+84.2}_{-51.3}$	$-2.9^{+23.4}_{-25.1}$	$-0.5^{+23.9}_{-25.2}$	$16.2^{+32.5}_{-35.8}$	$16.2^{+32.9}_{-35.1}$
15	$I_{\rm FeK\alpha}$ (10^{-5} photons cm^{-2} s^{-1})	$1.76^{+0.21}_{-0.20}$	$1.92^{+1.52}_{-0.57}$	$1.95^{+0.33}_{-0.32}$	$1.97^{+1.54}_{-0.47}$	$1.99^{+0.87}_{-0.44}$
16	EW$_{\rm Fe\ K\alpha}$ (eV)	38^{+5}_{-4}	43^{+34}_{-13}	43^{+7}_{-7}	51^{+40}_{-12}	51^{+22}_{-11}
17	σ_L (eV)	0.850 (f)	0.850 (f)	0.850 (f)	$149.4^{+42.5}_{-36.1}$	$149.6^{+42.6}_{-36.3}$
18	FWHM$_{\rm FeK\alpha}$ (km s^{-1})	100 (f)	100 (f)	100 (f)	17574^{+5001}_{-4252}	17604^{+5018}_{-4274}
19	$f_{\rm 2-10,c,obs}$ (10^{-11} erg cm^{-2} s^{-1})	2.87	3.15	3.16	2.53	2.53
20	$L_{\rm 2-10,c,rest,abso}$ (10^{44} erg s^{-1})	7.70	8.61	8.62	6.88	6.88
21	$L_{\rm 2-10,c,rest,unabso}$ (10^{44} erg s^{-1})	10.32	10.48	10.53	7.36	7.36
22	$f_{\rm 10-30,c,obs}$ (10^{-11} erg cm^{-2} s^{-1})	2.86	...	1.14	...	0.95
23	$L_{\rm 10-30,c,rest,abso}$ (10^{44} erg s^{-1})	7.94	...	9.34	...	11.46
24	$L_{\rm 10-30,c,rest,unabso}$ (10^{44} erg s^{-1})	7.86	...	8.07	...	4.94

Note. Columns (3)–(6) correspond to distinct fits. The contents of each row in these columns are labeled in Column 2 as follows: (1) Telescope and, in the case of *Suzaku*, ObsID for each individual fit; (2) detector(s) associated with data for each fit; (3) fit χ^2 and degrees of freedom (d.o.f.); (4) reduced χ^2 (χ^2_ν) for fit; (5) null fit probability ($P_{\rm null}$); (6) angle between torus symmetry axis and observer's line of sight; (7) $C_{\rm cross}$, i.e., either $C_{\rm PIN:XIS}$ (*Suzaku*) or $C_{\rm FPMB:FPMA}$ (*NuSTAR*); (8) $N_{\rm H}^{\rm inter}$, which gives the total column density of material intervening between the observer and the source; where fixed, this is the tabulated Galactic column density; (9) $N_{\rm H,Z}$, i.e., equivalent hydrogen column density associated with the single zeroth-order (direct) continuum in all cases, except for *Suzaku* observation 706, where it is associated with the partially covered zeroth-order continuum; (10) $N_{\rm H,S}$, equivalent hydrogen column density associated with the scattered (reflected) continuum and the fluorescent line emission component; (11) A_Z, only for *Suzaku* observation 706, is the relative normalization between fully and partially covering direct continua; (12) A_S, i.e., relative normalization between direct and scattered continuum; (13) Γ is the power-law slope; (14) $E_{\rm shift}$ is the energy shift of the Fe Kα model at the line peak in the observed frame; (15) Fe Kα line flux; (16) Fe Kα line EW; (17) Fe Kα line Gaussian width σ_L (see text); (18) Fe Kα line FWHM; (19) 2–10 keV continuum flux, observed frame; (20) 2–10 keV continuum absorbed luminosity, AGN frame; (21) 2–10 keV continuum unabsorbed luminosity, AGN frame; (22) 10–30 keV continuum flux, observed frame; (23) 10–30 keV continuum absorbed luminosity, AGN frame; (24) 10–30 keV continuum unabsorbed luminosity, AGN frame. Fixed parameters are indicated by (f).

only the direct power-law component. The energy ranges used were 2–10 and 10–30 keV.

3.7. Suzaku *XIS*

As stated, we fitted the two observational data sets 702 and 706 independently. For each observation, we first fitted only the combined XIS data with a baseline MYTORUS model. We discuss additional components introduced below.

Our strategy was first to step independently through each parameter until a preliminary stable solution was found. To avoid fitting instabilities that can be introduced by a weak emission line, we stepped through the line redshift parameter, z, with σ_L fixed at 8.5×10^{-4} keV (100 km s^{-1}, FWHM). After a stable minimum was obtained, z was fixed and σ_L was left free and stepped through to estimate the best-fit solution. If the lower 90% limit tended to $\sigma_L = 0$, σ_L was frozen at 100 km s^{-1} as the narrow line was not resolved.

For observation 702, $N_{\rm H,Z}$ converged to a value below the lower limit of MYtorusZ (10^{22} cm^{-2}). In this regime of column density $N_{\rm H,Z}$ has negligible Compton scattering so that simple absorption is sufficient. We thus replaced MYtorusZ with `zphabs` in the MYTORUS model.

The only additional component to the baseline MYTORUS model that led to a statistically significant improvement (probability less than 10^{-4} of data consistent with the model without the extra component) was Fe XXV emission at ~6.67 keV (rest frame). This was modeled by a `zgauss` component. The line is unresolved and thus fixed at 100 km s^{-1}. Such narrow emission lines are thought to originate in highly ionized gas far from the central SMBH and their presence is well documented in many Type 1 AGNs and is not surprising (e.g., Bianchi et al. 2004, 2009; Nandra et al. 2007; Patrick et al. 2011, 2012).

For observation 702, the full XSPEC model was thus

```
phabs *
(zphabs*zpowerlw
+constant*atable_mytorusS
+constant*gsmooth*atable_mytorusL
+zgauss).
```

For observation 706, we found that fixing the overall absorption between the observer and the source to the tabulated Galactic value still left a signature of excess extinction. We

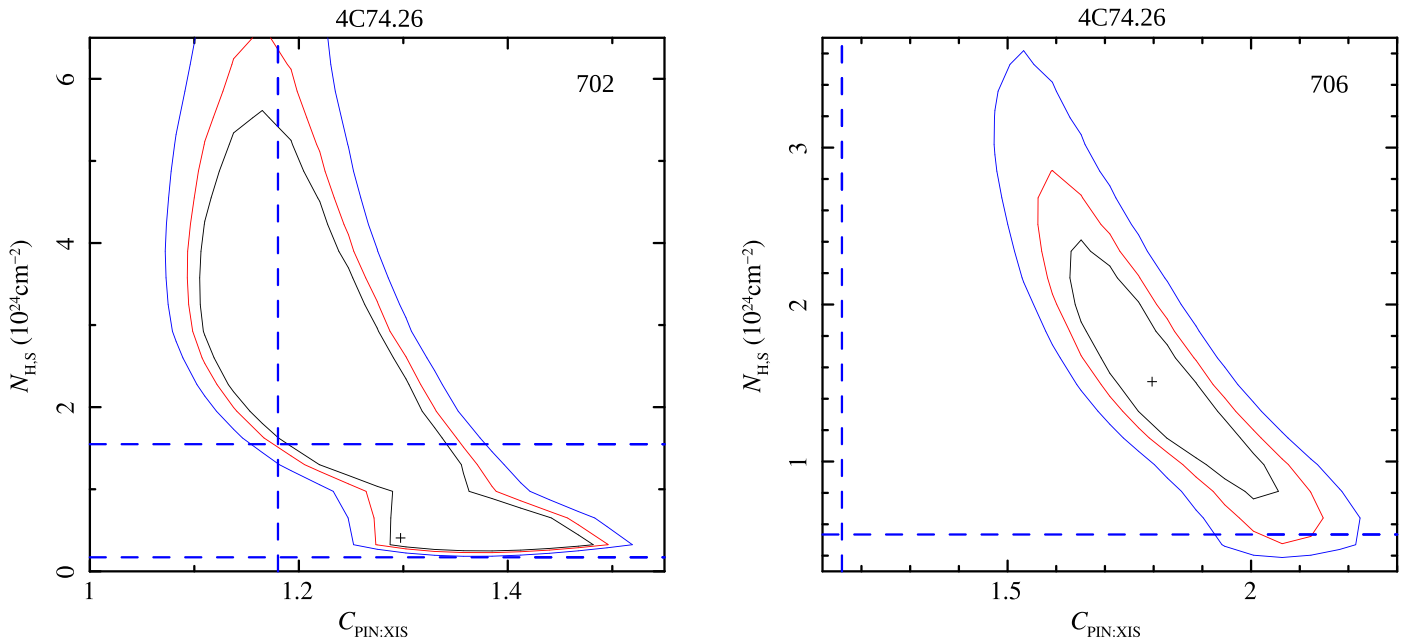

Figure 2. Determination of optimal cross-normalization, $C_{\rm PIN:XIS}$, for *Suzaku* XIS+PIN fits. Shown are contours of $N_{\rm H,S}$ from XIS+PIN MYTORUS fitting against $C_{\rm PIN:XIS}$ for observations 702 and 706. The horizontal lines mark the 90% bounds from the XIS-only best fit (only lower bound for 706), and the vertical lines the recommended $C_{\rm PIN:XIS}$ values of 1.18 (for 702) and 1.16 (for 706). Contours are shown at 68%, 90%, and 99% confidence.

thus let the corresponding `phabs` parameter be free, leading to an increase by a factor of about two. In addition, the ∼5–7 keV spectrum shows signs of significant line-of-sight absorption larger than at lower energies. To account for this the absorption was modeled to only partially cover the line of sight. This was implemented by means of a `zpowerlw` term for nonabsorbed emission and a `constant*etable_mytorusZ*zpowerlw` term for absorbed emission, where the first two components were allowed to be free, while the power law was tied to the other (nonabsorbing) power law of the model. Here, the `constant` component is the relative contribution of this additional power law (A_Z in Table 3). The full XSPEC model was thus

```
phabs *
(zpowerlw
+constant*etable_mytorusZ*zpowerlw
+constant*atable_mytorusS
+constant*gsmooth*atable_mytorusL).
```

3.8. Suzaku *XIS+PIN*

For the combined XIS+PIN fit, we investigated whether using the recommended values $C_{\rm PIN:XIS} = 1.18$ and 1.16 (for *Suzaku* observations 702 and 706, respectively) was reasonable. We obtained a preliminary best fit with $C_{\rm PIN:XIS}$ free, and then explored $N_{\rm H,S}$–$C_{\rm PIN:XIS}$ parameter space by means of two-dimensional contours as shown in Figure 2. In this figure the horizontal dashed lines mark the 90% $N_{\rm H,S}$ bounds from XIS-only fitting, while the vertical dashed lines mark the fiducial recommended $C_{\rm PIN:XIS}$ values of 1.16 and 1.18. In the case of observation 702 the upper 90% $N_{\rm H,S}$ bound intersects all three contour levels, and so does the line for $C_{\rm PIN:XIS} = 1.18$. The lower $N_{\rm H,S}$ bound intersects the 99% contour. We considered this satisfactory evidence that the value of 1.18 was adequate for this data set and we fixed the parameter to this value for the combined XIS+PIN fitting of the 702 observation. On the other hand, for observation 706 the vertical line for $C_{\rm PIN:XIS} = 1.16$ does not intersect any of the three contours, although the contours overlap with the $N_{\rm H,S}$ range from the XIS-only fit (which actually only has a lower limit in $N_{\rm H,S}$). We thus left $C_{\rm PIN:XIS}$ free in the combined XIS+PIN fit. Apart from the cross-normalization parameter, implemented with an extra `constant` component in XSPEC, the rest of the model components were as in the XIS case for each observation.

3.9. NuSTAR

We fitted the FPMA and FPMB data simultaneously, allowing their cross-normalization to be free by means of a cross-normalization parameter $C_{\rm FPMB:FPMA}$, implemented as a `constant` component in XSPEC. We fixed this parameter to unity for FPMA, and allowed it to be free for FPMB, thus obtaining the best-fit relative cross-normalization of FPMB with respect to FPMA.

Our fitting strategy for obtaining a preliminary stable solution involving the z and σ_L parameters was as described in Section 3.7 for *Suzaku*. As for *Suzaku* observation 702, we once more found it necessary to replace MYtorusZ with `zphabs` because with the former the $N_{\rm H,Z}$ value hit the model's lower bound. The full XSPEC model was thus

```
constant *
phabs *
(zphabs*zpowerlw
+constant*atable_mytorusS
+constant*gsmooth*atable_mytorusL).
```

4. Results and Discussion

Spectral fitting results for the 4C 74.26 *Suzaku* data (individual observations) and *NuSTAR* data (combined) with the MYTORUS model are shown in Table 3 and Figures 3–7.

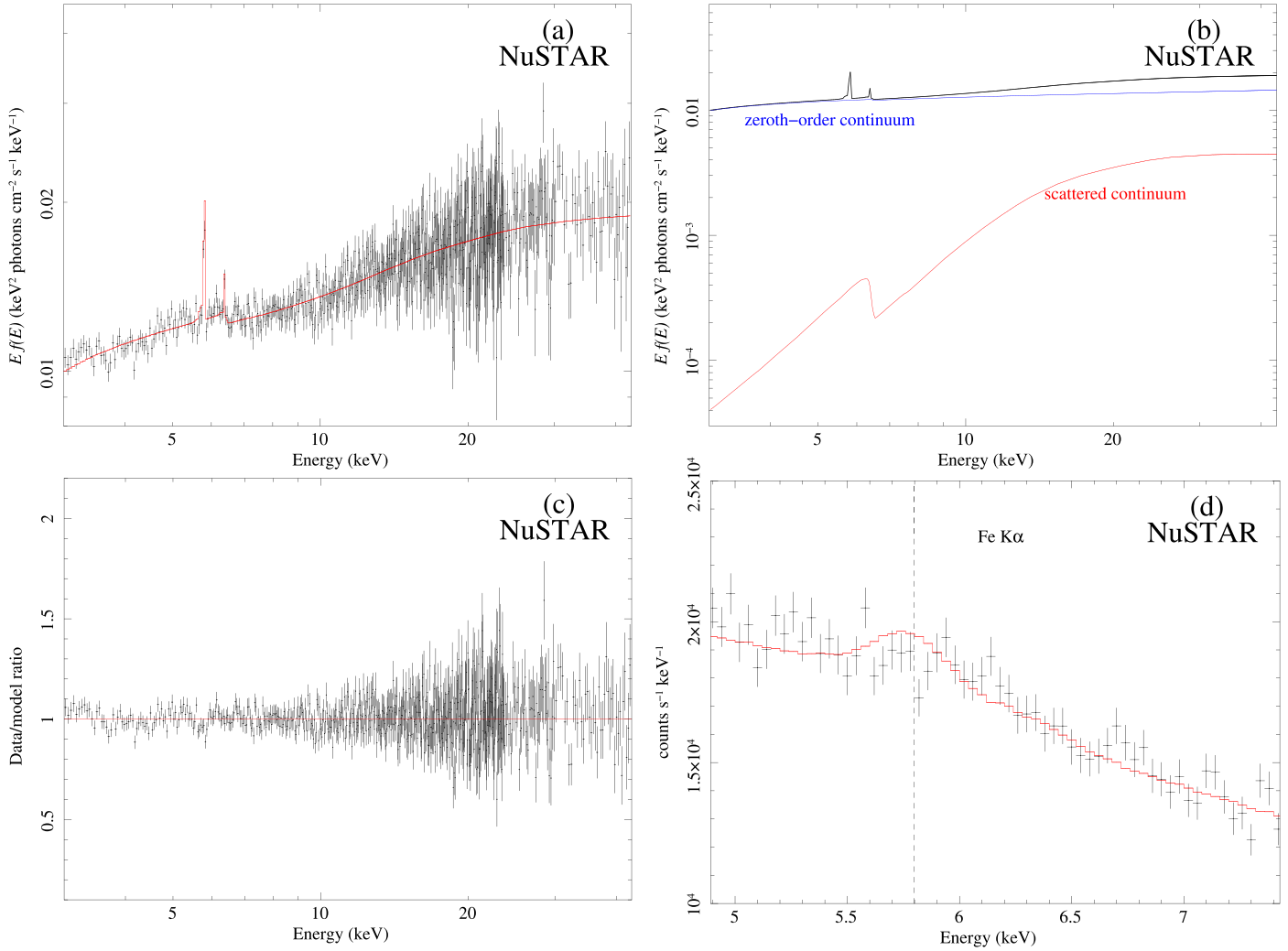

Figure 3. Results of spectral fitting of the co-added *NuSTAR* observations with MYTORUS. FPMA and FPMB results are combined for plotting purposes only. (a) Data and total model over the full spectral range fitted, (b) total model (black) and continuum components, (c) data/model ratio, and (d) data and total model in the vicinity of the Fe Kα emission line.

Column 2 in Table 3 lists the particular best-fitting parameters or information items that are shown in subsequent columns in the same row. These are explained in detail in the table caption. In the figures, panel (a) shows data and total best-fit model, (b) the total and individual continuum model components, (c) the data/model ratio, and (d) the data with total model in the vicinity of the Fe Kα line. In Table 3 the energy shift of the Fe Kα model relative to the reference energy ($6.400(1+z)$, $z \equiv 0.104$) is in the observed frame. The same applies to all continuum fluxes, to facilitate comparisons with values in the literature. On the other hand, continuum luminosities are in the AGN (i.e., rest) frame. All other parameters are in the AGN frame. We first present key points related to the spectral fitting for different data sets. We then discuss results for individual parameters in detail.

4.1. NuSTAR *Fit*

The *NuSTAR* fit is shown in Figure 3. Although we fitted the combined FPMA and FPMB data simultaneously without merging them, the FPMA and FPMB data and fit are shown combined for plotting purposes and to facilitate visualization of results. For both the FPMA and FPMB data the lower limit for the Fe Kα emission line σ_L was always zero, so we fixed σ_L at the equivalent of 100 km s^{-1}, FWHM, consistent with an unresolved narrow line.

4.2. Suzaku *Fits*

4.2.1. ObsID 702

Fitting results for this ObsID are plotted in Figures 4 and 5 for XIS and XIS+PIN, respectively. It can be seen from Columns (4) and (5) in Table 3 that the fitting results with and without the PIN data are similar. For $N_{\rm H,S}$, although the best-fitting value is $\sim$7 times higher for the XIS+PIN fit, both fits are consistent within the errors with a moderately Compton-thick global column density (see also Figure 2, left panel). The narrow-line component was unresolved and its width was fixed at 100 km s^{-1}, FWHM. In addition, in both cases we modeled emission from Fe XXV at $\sim$6.67 keV (rest), which must be from a completely distinct, highly ionized region (see also, e.g., Yaqoob et al. 2003; Bianchi et al. 2005; Patrick et al. 2012; Gofford et al. 2013).

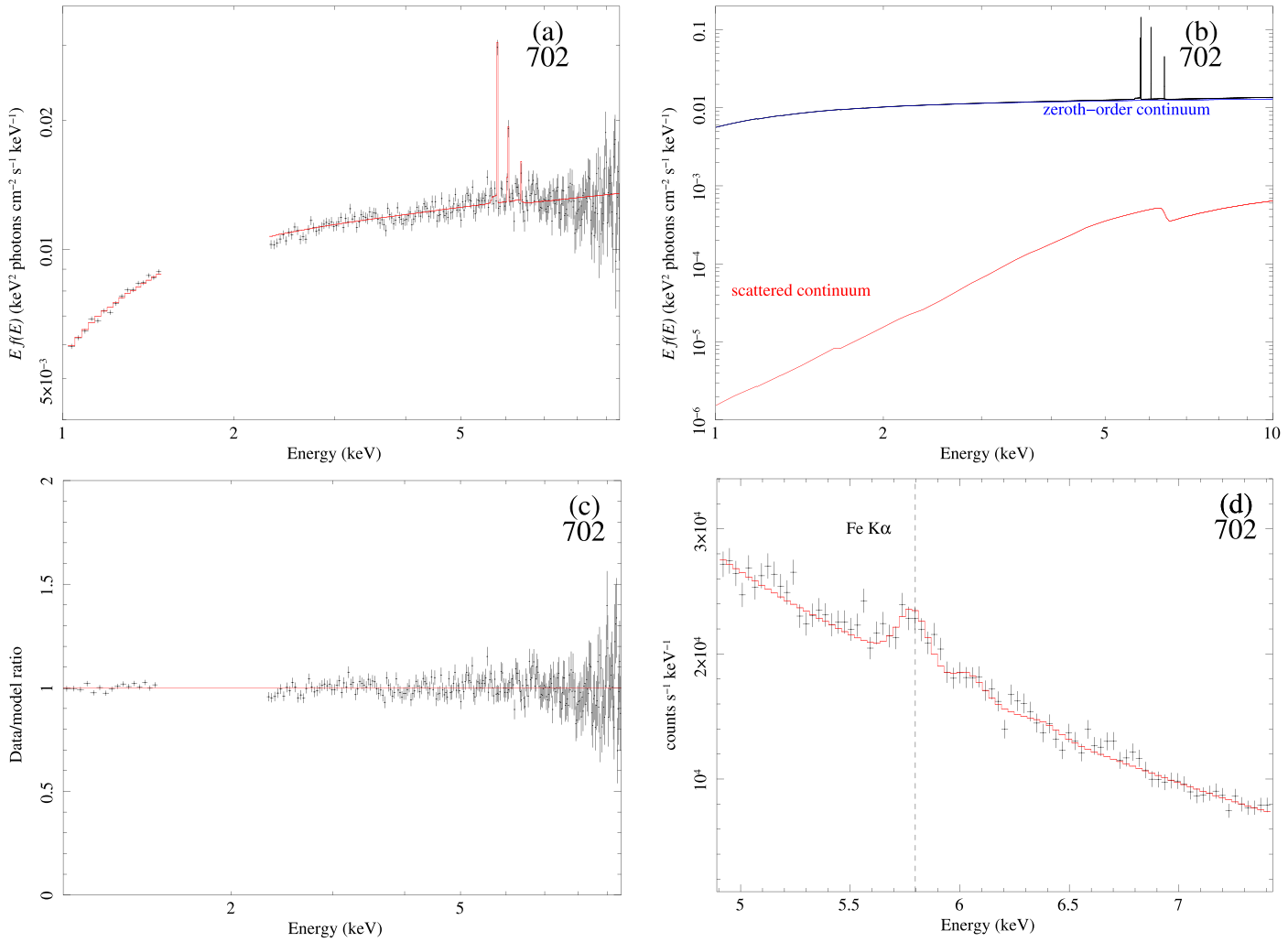

Figure 4. Results of spectral fitting to *Suzaku*-XIS ObsID 702 with MYTORUS. Panels are as in Figure 3.

4.2.2. *ObsID 706*

Fitting results for this ObsID are plotted in Figures 6 and 7. As in ObsID 702, the results with and without PIN are similar (see Columns (6) and (7) in Table 3, and Figure 2, right panel). The $N_{\rm H,S}$ best-fit value for the XIS+PIN fit is ∼3 times higher and better constrained than the lower limit for the XIS-only fit; however, within the errors they are consistent with each other, and with an overall Compton-thick column density out of the line of sight. As mentioned, we used two line-of-sight components for this observation to model partial coverage. While the non-covered component has no absorbing column density associated with it, the covered component (∼30%, Columns (6) and (7) in row (11), Table 3) has a column density of $\sim 14 \times 10^{22}$ cm^{-2}. This is the only observation for which the line component was resolved at ∼17,600 km s^{-1}, FWHM. In addition, for this observation we also found it necessary to keep the overall intervening absorption between observer and source ($N_{\rm H}^{\rm inter}$) free; it converged to a value larger than about twice the Galactic value.

4.3. Intrinsic Continuum

In Table 3 it can be seen that the photon index of the power-law intrinsic continuum, Γ, is similar across observations and instruments, ranging from ∼1.9 to ∼2, and does not appear to be sensitive to either $C_{\rm PIN:XIS}$ or spectral range (XIS-only versus XIS+PIN or *NuSTAR*). A value of ∼1.9 is typical for intrinsic X-ray continua of Type 1 AGNs (e.g., Dadina 2007; Nandra et al. 2007).

4.4. X-Ray Reprocessor Column Densities

The most common methodology for determining whether an AGN is Compton-thick estimates only the line-of-sight column density. In models such as `pexrav` or `pexmon` the column density associated with reflection is assumed to be infinite; a *global* column density is absent. This is thus the first time that the global average column density, out of the line of sight, has been measured in this object. This is particularly noteworthy because we find the two types of column density to be significantly different. All line-of-sight column densities for all observations are well in the Compton-thin regime, ranging from $\sim 0.19 \times 10^{22}$ to $\sim 14 \times 10^{22}$ cm^{-2} (row (9) in Table 3). In contrast, all global column densities from broadband data (*Suzaku* XIS+PIN and *NuSTAR*) are unambiguously Compton-thick, ranging from ∼1.5 to $\sim 2.9 \times 10^{24}$ cm^{-2}, while within the uncertainties even those derived from XIS only are consistent with being Compton-thick (row (11) in Table 3). It is important to note also that the shape of the reflection spectrum for the global column densities found here is significantly different from that due to extremely Compton-thick matter with

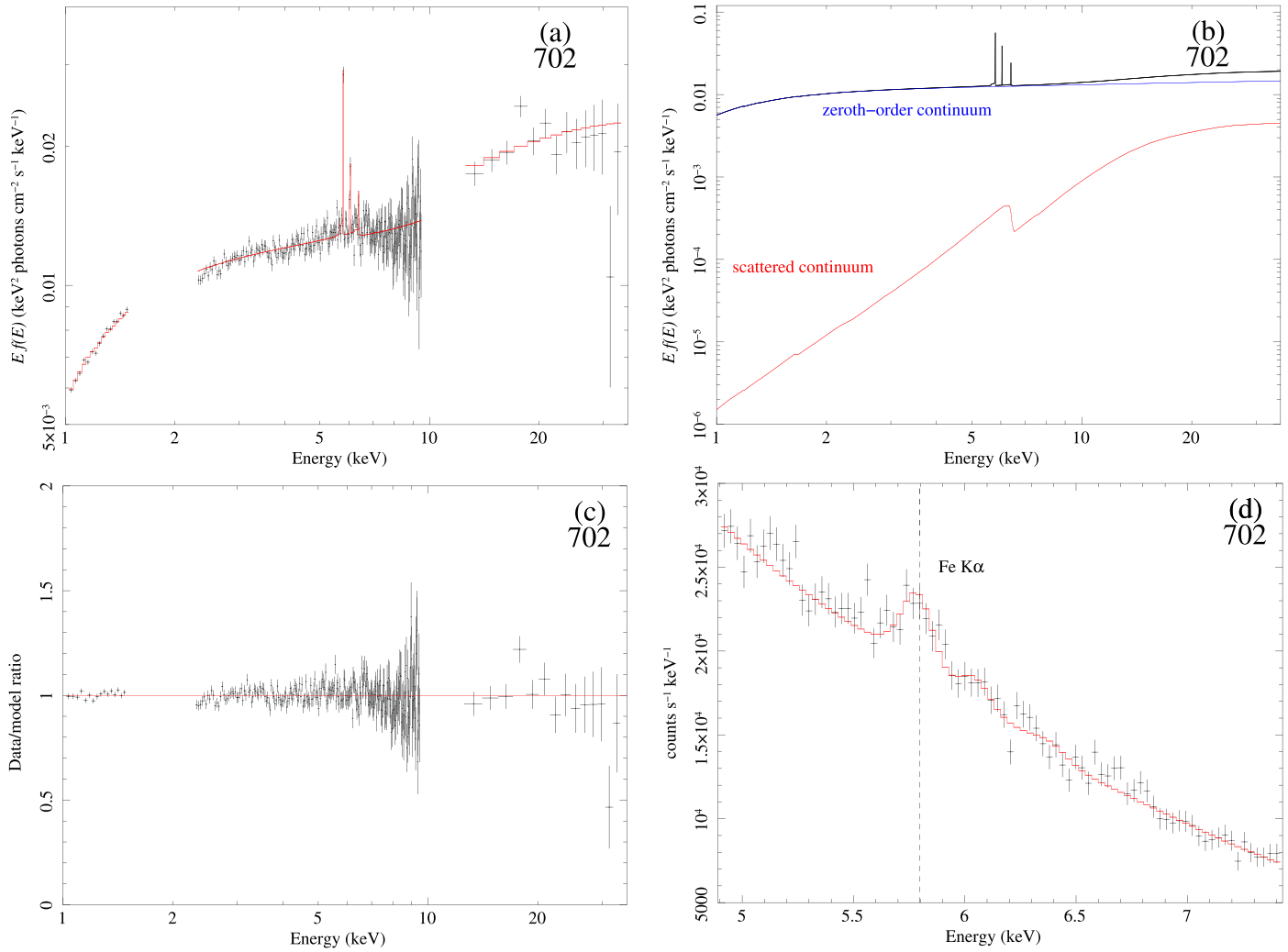

Figure 5. Results of spectral fitting to *Suzaku*-XIS+PIN ObsID 702 with MYTORUS.Panels are as in Figure 4.

column densities $\gg 10^{25}$ cm^{-2} (which is the case for the disk-reflection models with infinite column density such as `pexrav` or `pexmon`). It is then to be expected that our results may differ markedly from such entirely different analyses. Only some works that adopt such different analysis strategies have reported (single, line-of-sight) values of equivalent hydrogen column density. These range from $<3.1 \times 10^{20}$ cm^{-2} (Fukazawa et al. 2011) to $>6.2 \times 10^{21}$ cm^{-2} (Gofford et al. 2013), and would clearly lead to Compton-thin classifications.

4.5. Continuum Fluxes and Luminosities

In Table 3 the observed (absorbed) 2–10 keV fluxes are very similar for ObsID 702 with XIS and with XIS+PIN (3.15 versus 3.16×10^{-11} erg cm^{-2} s^{-1}), and similarly for luminosities. The *NuSTAR* flux value is somewhat lower (2.87×10^{-11} erg cm^{-2} s^{-1}), while values for the ObsID 706 are somewhat lower still (2.53×10^{-11} erg cm^{-2} s^{-1}). These ranges anticorrelate with the ranges in line-of-sight column density $N_{\rm H,Z}$, which is highest for ObsID 706, and lowest for ObsID 702. The unabsorbed 2–10 keV luminosities are more similar between *NuSTAR* and ObsID 702 XIS and XIS+PIN, but ObsID 706 (XIS and XIS+PIN) is still lower, as in the absorbed case. This then might suggest that in this range the emitted flux and luminosity were intrinsically lower for the 706 observation. This is consistent with the findings of Tombesi et al. (2014) but in disagreement with Lohfink et al. (2017, their Figure 1).

In the energy range 10–30 keV there are no similar trends either for absorbed or for unabsorbed fluxes or luminosities. Note that the intrinsic (unabsorbed) 10–30 keV luminosities are somewhat lower than their absorbed counterparts, since the latter also include reflection from the torus, which increases the apparent luminosity.

4.6. Fe Kα Emission Line

The best-fit energy shift of the Fe Kα line peak in Table 3 ranges from $-0.5^{+23.9}_{-25.2}$ to $16.2^{+32.9}_{-35.1}$ eV. The largest values are for Suzaku-706 XIS and XIS+PIN data, and are likely due to systematic effects in the XIS energy scale, and perhaps some mild ionization, although all values are consistent with zero shift within their 90% errors. In any case, any such level of ionization is negligible and the assumption of an essentially neutral reprocessor is robust.

Looking at the zoomed-in Fe Kα regions for the *Suzaku* data in Figures 4(d) and 5(d), which have the highest energy resolution, it is remarkable that the narrow-line MYTORUS model for ObsID 702 data provides an excellent fit to the

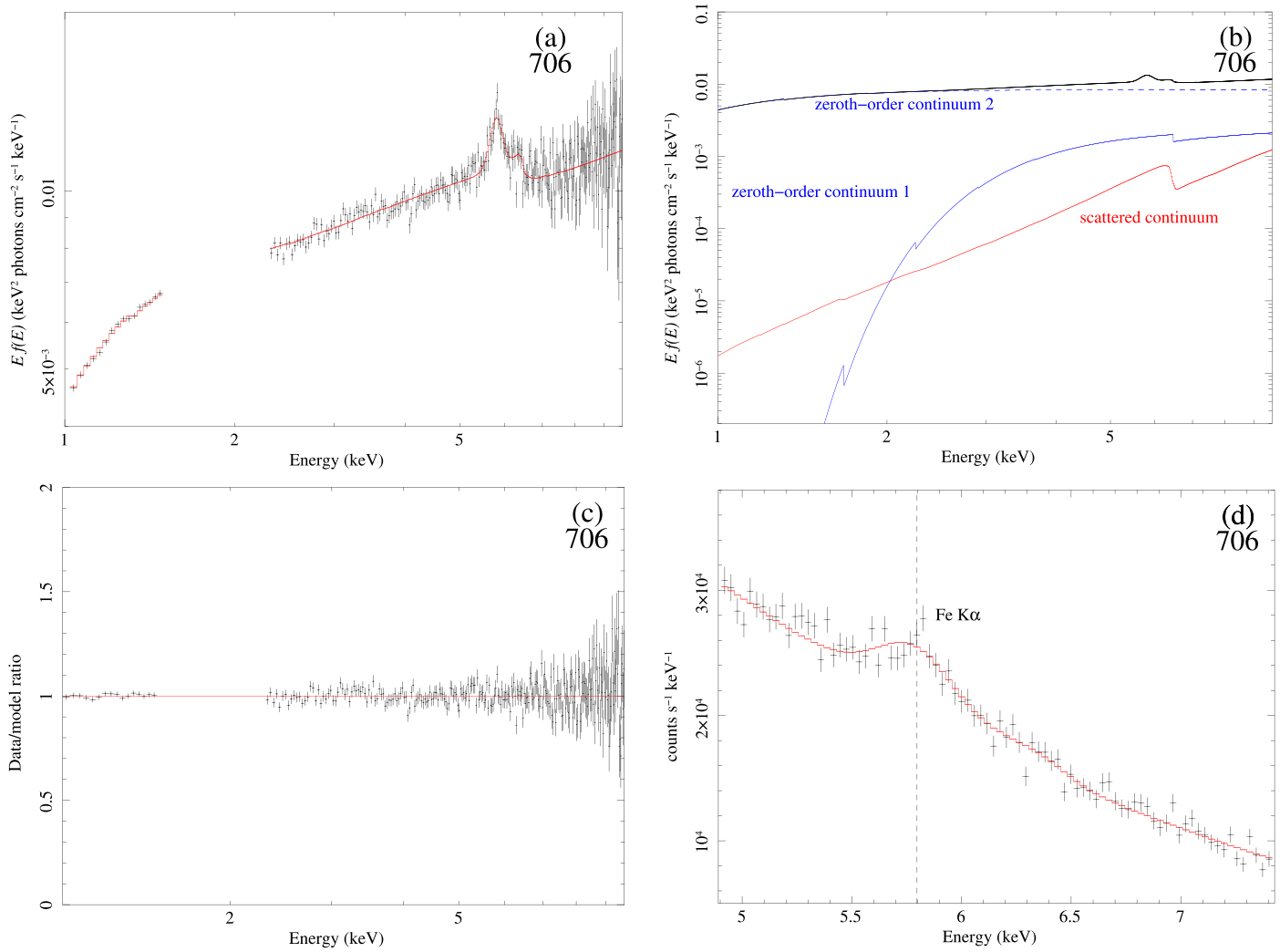

Figure 6. Results of spectral fitting to *Suzaku*-XIS ObsID 706 with MYTORUS. Panels are as in Figure 4.

Fe Kα line, even though the line is not resolved (see also the plots of residuals (c) in the same figures). For the ObsID 706 data, the only data set in which the line is resolved, an excellent fit is also obtained with only a narrow, although broader, line (Figures 6(c), (d) and 7(c), (d), and Table 3). The best-fit σ_L is $\sim$150 eV or FWHM $\sim$ 17,650 km s^{-1}.

We can obtain a rough estimate of the size of the emitting region if we assume Keplerian motion. As in Shu et al. (2011), we assume that the line-emitting matter is virialized and orbits the black hole. The distance r to a black hole of mass $M_\bullet$ is then given by $GM_\bullet = r\langle v^2\rangle$, where G is the gravitational constant and $\langle v^2\rangle$ the velocity dispersion. We further assume that v is related to FWHM velocity by $\langle v^2\rangle = \frac{3}{4}\,\mathrm{FWHM}^2_{\mathrm{FeK}\alpha}$ (Netzer et al. 1990), obtaining $r = \frac{4c^2}{3\,\mathrm{FWHM}^2_{\mathrm{FeK}\alpha}}\,r_g$, where the gravitational radius is $r_g \equiv GM_\bullet/c^2$. We set $M_\bullet = 4\times10^9\,M_\odot$ (Woo & Urry 2002) and use the $\mathrm{FWHM}_{\mathrm{FeK}\alpha}$ range of values in Table 3. We only carry out this exercise for *Suzaku* observation 706 (Columns (6) and (7) in row 19 of Table 3) in which the line is resolved, taking the upper and lower $\mathrm{FWHM}_{\mathrm{FeK}\alpha}$ limits into account. The resulting size range is $\sim$230 to $\sim$680 r_g ($\sim$0.045 to $\sim$0.13 pc) for the Fe Kα emitting region. In addition, using the relation of Peterson et al. (2004) for the size of the *optical* broad-line region (BLR) for a $4\times10^9\,M_\odot$ SMBH, the Hβ emission line widths of Corbin (1997) and Brinkmann et al. (1998) of 11,000 km s^{-1} and 4700 km s^{-1}, FWHM, produce estimates for the radius R_{BLR} of 0.14 and 0.78 pc, respectively. These correspond to $\sim$740 and $\sim$410 r_g, respectively. The Fe Kα emitting region is then likely to be at least partially coincident with, and possibly inside, the BLR.

While a range of values $\sim$230–680 r_g are lower than the *median* estimate of Shu et al. (2011) ($3\times10^4 r_g$) for narrow Fe Kα AGNs, this is well beyond the strong-gravity regime, which would require less than $\sim$50 r_g (e.g., Fabian et al. 1989; Reynolds & Nowak 2003). In addition, the estimates for the relative sizes of the Fe Kα and optical broad-line emitting regions are entirely consistent with Shu et al. (2011), who found that the narrow Fe Kα line is likely to arise in a region within a factor of $\sim$(0.7–11) $\times$ R_{BLR}. The fact that the line appears broader in this observation than in the others may be a combination of several effects. It is well known in the optical that AGN emission lines can change even as far as leading to Type 1 AGNs being reclassified as Type 2 ("changing look" AGNs, e.g., LaMassa et al. 2015 and references therein). In the X-rays, the Fe Kα line shape, which depends on the global distribution of scattering material, cannot change only under the effect of motion, since, overall, the same amount of matter should be present between observations. Rather, the observed

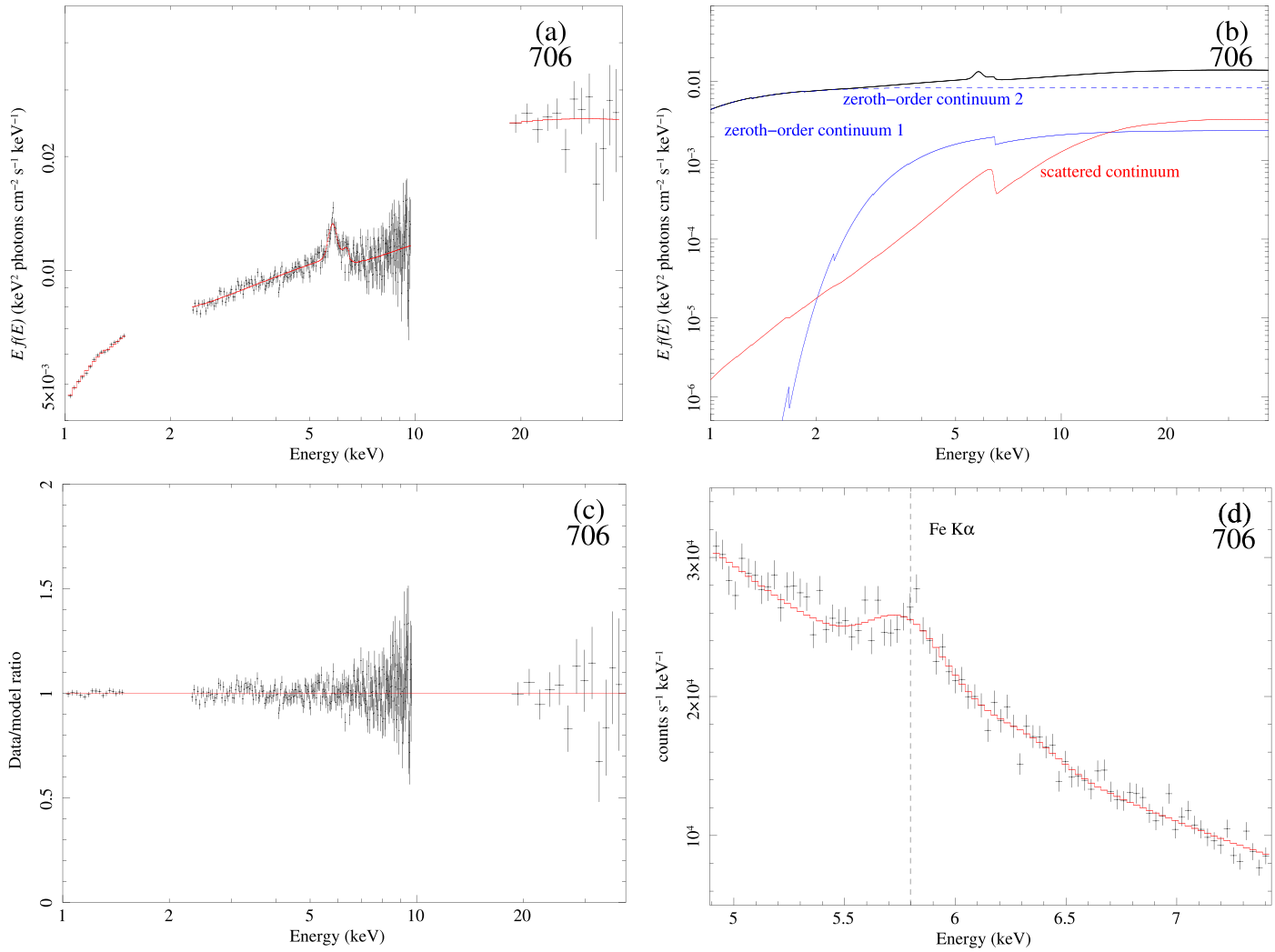

Figure 7. Results of spectral fitting to *Suzaku*-XIS+PIN ObsID 706 with MYTORUS.Panels are as in Figure 4.

change should be due to thermodynamics and/or ionization effects, which control the amount of neutral material. A change in the average distance of fluorescent and scattering matter will have an effect in this respect, because with varying distance the level of ionization will change. Further, the broadest part of the narrow line may come from the outer parts of the disk, perhaps a wind for which we know that the amounts of both matter and ionization can be variable. Note also that this observation combines the longest *Suzaku* exposure time and highest spectral resolution, while fixing the width in the other observations, where the line is not resolved, to 100 km s^{-1} is somewhat arbitrary. The line could be broader than that (but still below the resolution limit) so that, in fact, the discrepancy with the 706 width might be smaller.

Finally, the line fluxes and EWs are all consistent with each other across instruments and observations, ranging from $1.76^{+0.21}_{-0.20}$ to $1.99^{+0.87}_{-0.44} \times 10^{-5}$ photons cm^{-2} s^{-1} and 38^{+5}_{-4} to 51^{+40}_{-12} eV, respectively.

For observation 706, the resolved Fe Kα line is somewhat broad; we also estimated above that the emission may be at least partially occurring inside the BLR. The emission might then be coming from a truncated accretion disk, as suggested by Tombesi et al. (2014), who modeled this observation with a relativistically blurred (`kdblur`) `pexmon` component. Bhatta et al. (2018) also reported evidence for a truncated accretion disk after modeling the longest *NuSTAR* observation with `relxill`. To test this hypothesis, we modeled the XIS+PIN data of this observation with `relxill` (Dauser et al. 2014; García et al. 2014, version 1.2.0) and the model setup of Bhatta et al. (2018), i.e., `constant*tbabs*warmabs*relxill`, where as before the `constant` component accounts for XIS versus PIN cross-normalization. We adopted the assumptions of Bhatta et al. (2018) for Galactic column density (2.31×10^{21} cm^{-2}) and `warmabs`, i.e., outflow velocity of 3600 km s^{-1}, column density 3.5×10^{21}cm^{-2}, ionization parameter 2.6 in the log, and turbulent velocity 100 km s^{-1}. For the purposes of comparison with these two previous works we assumed a uniform emissivity index of 3, a maximally spinning black hole, solar iron abundance, and cutoff energy of 180 keV. We first imposed the further assumptions of an outer disk radius $R_{\rm out} = 400 r_g$ and disk inclination angle 30° (Tombesi et al. 2014). This produced a best fit with an inner disk radius of $R_{\rm in} = 32^{+14}_{-12}\, r_g$ and reflection fraction $R = 0.41^{+0.05}_{-0.04}$, consistent with the results of Tombesi et al. (2014). However, the fit is rather poor ($\chi^2_\nu = 1.3$, $P_{\rm null} = 3 \times 10^{-4}$). Modifying the model setup by fixing $R_{\rm out} = 1000\, r_g$ and a disk inclination angle of 45° (Bhatta et al. 2018) only produced a poor best fit, with $\chi^2_\nu = 1.5$ and $P_{\rm null} = 1 \times 10^{-8}$. Modifying

this model setup by relaxing the requirement for uniform emissivity leads to an improved fit ($\chi^2_\nu = 1.2$, $P_{\rm null} = 0.01$) with an inner disk emissivity index of 5^{+2}_{-1} and an outer disk index of $0.8^{+0.5}_{-1.1}$ for an assumed break radius of $20\,r_g$. This result, however, is not consistent with a truncated disk ($R_{\rm in} = 2.2^{+0.6}_{-0.3}\,R_{\rm ISCO}$). We note that this result is at least qualitatively consistent with theoretical modeling predictions that favor a much steeper emissivity profile in the inner accretion disk (Wilkins & Fabian 2011, 2012; Gonzalez et al. 2017).

In conclusion, relatively simple, standard MYTORUS configurations that model a narrow Fe Kα emission line at 6.4 keV and its associated reflection continuum originating in neutral matter far from the accretion disk with solar Fe abundance are entirely able to provide excellent fits to all the data. None of the observations provides any statistical evidence for an additional relativistically broadened Fe Kα emission line. However, the Suzaku-706 observation, where a $\sim$17,000 km s^{-1} emission line is resolved, can alternatively be modeled exclusively by a relativistically broadened component, consistent with a maximal black hole spin value, as in earlier results.

To our knowledge, this is the first time that data for 4C 74.26 have been fitted with narrow-only Fe Kα emission, using a physically motivated model such as MYTORUS, which self-consistently models both Fe Kα line emission and the reflection continuum, and uses only solar abundances. In addition, previous works that have analyzed these *Suzaku* and *NuSTAR* data commonly start with the assumption that there is a broad component of the Fe Kα line, motivated by simple power-law residual plots (e.g., Figure 5 in Larsson et al. 2008 and Figure 3 in Patrick et al. 2012 for *Suzaku* ObsID 702; Figure 2 in Lohfink et al. 2017 for the average FPMA/B *NuSTAR* data; see also Figure 1 in Ballantyne & Fabian 2005 for *XMM-Newton* data). They then proceed to model the broad line by including relativistic components, which can lead to estimates of black hole spin (Lohfink et al. 2017). Any additional narrow Fe Kα component is routinely added as an additional ad-hoc Gaussian, which is completely different to the self-consistent Fe Kα line emission and associated reflection continuum of MYTORUS. Our starting point was entirely different in that we first modeled the simplest, less exotic case of narrow-line Fe Kα emission to assess how well it can fit the data without a broad component. If there were a prominent broad feature, such a model should fail to provide even a moderately good fit. We found that this is not the case, contradicting previous results.

The particular case of *Suzaku* ObsID 702 is noteworthy. The majority of previous analyses of this ObsID found a broad line, with σ values reported as high as 240–300, $<$190, and $\sim$270 eV (Larsson et al. 2008; Patrick et al. 2012; Gofford et al. 2013, respectively). This would mean that *Suzaku* resolved the line. In contrast, our analysis shows that the line is not resolved, and our fitting process (Section 3.7) justified fixing the line to a mere 100 km s^{-1}, FWHM, leading to an excellent fit as is evident in Figures 4(d) and 5(d).

Given that the *Suzaku* data, which have higher energy resolution than *NuSTAR*, do not support a broad-line component, and that the lower σ_L limit for the *NuSTAR* data is zero, our results are unable to confirm those of Lohfink et al. (2017), who report σ_L of $0.57^{+0.09}_{-0.08}$ keV for the same *NuSTAR* data. We are then forced to conclude that such a value might be an artefact of data quality that leads to a broad-line model component partly modeling the continuum instead of a bona fide broad line.

5. Summary and Conclusions

We extracted X-ray spectra from two *Suzaku* and four merged *NuSTAR* X-ray observations of the quasar 4C 74.26 to test the hypothesis that these X-ray spectra can be fitted exclusively with a narrow Fe Kα emission line and associated reflected continuum. A prominent broad line has been claimed in several earlier works, including some that are based on the same data as in the present work, and this Type 1 AGN has a relatively simple X-ray spectrum, making it an ideal test case.

We fitted the spectra with MYTORUS, which self-consistently models the Fe Kα line emission and associated reflected continuum from material of finite column density with solar Fe abundance. We fitted *NuSTAR* FPMA and FPMB data simultaneously with free cross-normalization, and estimated the best cross-normalization factor $C_{\rm PIN:XIS}$ for *Suzaku* XIS +PIN data. Our key results are as follows.

1. For all data, regardless of telescope or instrument, we obtained excellent fits ($\chi^2_\nu \sim 1$) with narrow-only Fe Kα line emission and associated reflected continuum.
2. Our fits require only solar Fe abundance in an X-ray reprocessor with finite column density, far from the central SMBH.
3. For the first time, we measured the global column density associated with Compton scattering out of the line of sight ($N_{\rm H,S}$) independently of the line-of-sight column density ($N_{\rm H,Z}$). For all observations, while $N_{\rm H,S}$ is in the Compton-thick regime ($\sim$1.5 to $\sim 2.9 \times 10^{24}$ cm^{-2}), $N_{\rm H,Z}$ is Compton-thin ($\sim 0.19 \times 10^{22}$ to $\sim 14 \times 10^{22}$ cm^{-2}). This has important implications for estimates of the fraction of Compton-thick AGNs in the universe, which routinely use only values for line-of-sight equivalent hydrogen column density.
4. The Fe Kα line is not resolved, with the exception of *Suzaku* ObsID 706 (FWHM $\sim$ 17,600 km s^{-1}). This observation can alternatively be modeled with a relativistic model with a broken power-law emissivity. However, two different model setups for a truncated accretion disk are not favored by the data.
5. Simple estimates suggest the size of the Fe Kα emitting region is $\sim$230 to $\sim$680 gravitational radii from the central SMBH, well beyond the strong-gravity regime.
6. Our results suggest that X-ray reprocessing in these data does not arise in the strong-gravity regime in the inner part of the accretion disk, and thus cannot constrain black hole spin.

For the *Suzaku* ObsID 706 data, further modeling of a possibly truncated accretion disk, motivated by the lower-limit estimate for the size of the Fe Kα emitting region, is beyond the scope of this paper, which explores whether a purely nonrelativistic model such as MYTORUS is able to fit these data. We do note though that the great majority of previous claims for relativistic broadening are based on the *Suzaku* ObsID 702 and *NuSTAR* data (see the Appendix). Our modeling results show that in these cases there is no hint of even a moderately broad line, thus providing no support for even exploratory relativistic modeling.

Fairall 9 is another AGN that was widely thought to show a relativistically broadened Fe Kα emission line in its X-ray spectra until it was recently modeled successfully with only a narrow line and its associated reflected continuum, all with solar Fe abundance (Yaqoob et al. 2016). In the case of 4C

74.26, only two previous works (Brinkmann et al. 1998; Noda et al. 2013) reported narrow-only Fe Kα line emission. Given the far-reaching implications of detecting Fe Kα emission originating in the inner part of the accretion disk, the possibility of less exotic, mundane modeling with narrow Fe Kα emission should be carefully considered, while the case for SMBH spin measurements remains open.

We thank the anonymous referee for his/her constructive comments that helped improve the paper. P.T. acknowledges support from NASA grant 80NSSC18K0408 (solicitation NNH17ZDA001N-ADAP). This work made use of data from the *NuSTAR* mission, a project led by the California Institute of Technology, managed by the Jet Propulsion Laboratory and funded by the National Aeronautics and Space Administration. This research made use of the *NuSTAR* Data Analysis Software (NuSTARDAS) jointly developed by the ASI Science Data Center (ASDC, Italy) and the California Institute of Technology (USA). This research has made use of data obtained from the *Suzaku* satellite, a collaborative mission between the space agencies of Japan (JAXA) and the USA (NASA).

Facilities: Suzaku, *NuSTAR*.

Appendix
Overview of Previous Results

For reference, we present here a further detailed overview of previous results for 4C 74.26.

The object features prominent 10′ radio lobes (Riley et al. 1989) and a one-sided radio jet (Riley & Warner 1990). Based on the jet asymmetry at parsec scales, Pearson et al. (1992) estimated a jet inclination of $\lesssim$49° to the line of sight.

Fe Kα line emission was first detected with *ASCA* (Brinkmann et al. 1998; Sambruna et al. 1999; Reeves & Turner 2000), and later with *BeppoSAX* (Hasenkopf et al. 2002). While Brinkmann et al. (1998) detected only a narrow line with $\sigma \sim 90$ eV using *ASCA*, Sambruna et al. (1999) reported a broad line with $\sigma \sim 590$ eV and EW ~ 215 eV. For all *ASCA* and *BeppoSAX* observations, Hasenkopf et al. (2002) quote EW ~ 200 eV with uncertainties of a factor of $\sim$2 and strong Compton reflection components.

In more recent results, Ballantyne & Fabian (2005) presented evidence that the *XMM-Newton* 2004 EPIC-pn observation shows a broad (EW $\sim$ 130–300 eV) ionized Fe Kα line extending very close to a maximally spinning black hole. Their best-fit model (2–12 keV) was a relativistically blurred ionized disk with an unblurred neutral reflector (Ross et al. 1999) and an additional narrow Gaussian emission line. Ballantyne (2005) extended this analysis down to 0.3 keV, and also reported evidence for excess cold absorption compared to the Galactic value, as well as warm absorption, but no soft excess.

Larsson et al. (2008) analyzed a *Suzaku* observation (ObsID 702057010; "B" in Tombesi et al. 2014), finding evidence for $\sim$20% flux increase during the observation. Their best-fitting model for ionized reflection with relativistic blurring reported broad (EW $\gtrsim$ 80 eV) Fe Kα line emission originating beyond $50r_g$ and a line-of-sight inclination of $\sim$20°. This led to the suggestion of an inner truncated accretion disk. They further concluded that a narrow component was not required since it led to only a marginal improvement of their fit.

For the same *Suzaku* observation, Patrick et al. (2012) fitted a broad Fe Kα line at 6.1 keV with a Gaussian ($\sigma < 0.19$ keV, EW $\sim$ 22 eV), and also found Fe XXV emission. However, their `relline` fit was unable to constrain black hole spin. Gofford et al. (2013) also analyzed this *Suzaku* observation. Using `reflionx`, they fitted a narrow Fe Kα line ($\sigma = 10$ eV) at 6.33 keV; they fitted broad Fe Kα line emission with a Gaussian ($\sigma \sim 270$ eV). The EWs for these were $\sim$13 and 47 eV, respectively. They included two warm absorbers from XSTAR modeling, and detected a single absorption trough at $E > 8$ keV, which they interpreted as an ultra-fast outflow (UFO, $\sim 0.2c$), although the specific ion identifications may be ambiguous ("degenerate XSTAR solutions"), and the statistical detection is marginal.

Noda et al. (2013) also analyzed this observation, reporting soft X-ray absorption above the Galactic value. They fitted time-resolved soft and hard excess emission, as well as the time-averaged spectra. Although they obtained good fits with several phenomenological models, they concluded that relativistically smeared ionized reflection (`kdblur*reflionx +pexrav`) could not provide an adequate model for the excesses. Instead, for their sample, they concluded that the soft excess was consistently well modeled by a thermal Comptonization component separate from the main power-law continuum. Thus the strong excess was deemed likely to arise in a distant cold reflector. The Fe Kα line had $\sigma = 10^{-4}$ keV (fixed) and EW $\sim$ 30–37 eV, depending on the model.

Tombesi et al. (2014) analyzed the *XMM-Newton*/EPIC-pn observation ("A") and another *Suzaku* observation ("C," 706028010). For obs. A, they used `xillver` to fit Fe Kα line emission at $\sim$6.5 keV as well as an ionized reflection component, and XSTAR tables for two warm absorber components. They fitted absorption at $E_{\rm rest} \sim 7.3$ keV with a Gaussian, and identified it as due to a UFO ($\sigma_v < 12{,}000$ km s^{-1}, $v_{\rm out} = 13{,}500 \pm 2400$ km s^{-1}). They obtained several possible best fits for obs. C, including (1) neutral Fe Kα line emission (`pexmon`) with two warm absorbers (XSTAR), and broad absorption consistent with a UFO; (2) redshifted broad neutral Fe Kα line emission from reflection off the accretion disk (`pexmon+kdblur`) consistent with a truncated disk; (3) ionized partial covering absorption (`zxipcf`).

Di Gesu & Costantini (2016) fitted the *XMM-Newton*/EPIC-pn observation with a phenomenological model, detecting excess soft X-ray absorption compared to the Galactic value. They further performed a combined spectral analysis using the *Chandra* High Energy Transmission Grating Spectrometer (HETGS) and *XMM-Newton* Reflection Grating Spectrometer (RGS, 0.4–2.0 keV). The HETGS data came both from the medium-energy grating (MEG, 0.7–6.2 keV) and the high-energy one (HEG, 2.5–8.3 keV). For their joint HETGS+RGS fit, absorption components were tied but continua were left to vary. The model was a phenomenological modified blackbody with a broad Gaussian Fe Kα line emission line (FWHM $\sim$ 0.16 Å, consistent with other *XMM-Newton*-based results). Several soft X-ray absorption features were also included, and a highly ionized warm absorber was also fitted, corresponding to an outflow velocity of $\sim$3600 km s^{-1}.

Lohfink et al. (2017) performed a joint analysis of *NuSTAR* with simultaneous *Swift*/XRT snapshots. Their best model included `pexmon` for cold reflection, and `relxilllpCp` combining relativistically blurred ionized reflection and a thermal Comptonization continuum. They measured a high-energy cutoff of 183^{+51}_{-35} keV, and reported ionized reflection, a mildly ionized warm absorber, excess cold absorption $<2 \times 10^{21}$ cm^{-2}, and a broad Fe Kα line with equivalent

width ∼200 eV and $\sigma = 0.57^{+0.09}_{-0.08}$ keV. They reported spin values constrained to >0.5.

Bhatta et al. (2018) modeled the longest (∼90 ks) *NuSTAR* observation with `relxill` for a maximally spinning SMBH, with a cutoff energy of 180 keV and solar iron abundance. They obtained an inner accretion disk radius of $\sim 35 R_{\rm ISCO}$, suggesting a truncated accretion disk.

ORCID iDs

P. Tzanavaris https://orcid.org/0000-0001-5737-5055
S. LaMassa https://orcid.org/0000-0002-5907-3330
A. Ptak https://orcid.org/0000-0001-5655-1440

References

Anders, E., & Grevesse, N. 1989, GeCoA, 53, 197
Antonucci, R. 1993, ARA&A, 31, 473
Arnaud, K. A. 1996, in ASP Conf. Ser. 101, Astronomical Data Analysis Software and Systems V, ed. G. H. Jacoby & J. Barnes (San Francisco, CA: ASP), 17
Ballantyne, D. R. 2005, MNRAS, 362, 1183
Ballantyne, D. R., & Fabian, A. C. 2005, ApJL, 622, L97
Baloković, M., Brightman, M., Harrison, F. A., et al. 2018, ApJ, 854, 42
Baronchelli, L., Nandra, K., & Buchner, J. 2018, MNRAS, 480, 2377
Bhatta, G., Stawarz, Ł., Markowitz, A., et al. 2018, ApJ, 866, 132
Bianchi, S., Guainazzi, M., Matt, G., Fonseca Bonilla, N., & Ponti, G. 2009, A&A, 495, 421
Bianchi, S., Matt, G., Balestra, I., Guainazzi, M., & Perola, G. C. 2004, A&A, 422, 65
Bianchi, S., Matt, G., Nicastro, F., Porquet, D., & Dubau, J. 2005, MNRAS, 357, 599
Blandford, R. D., & Znajek, R. L. 1977, MNRAS, 179, 433
Brenneman, L. 2013, Measuring the Angular Momentum of Supermassive Black Holes (New York: Springer)
Brenneman, L. W., & Reynolds, C. S. 2009, ApJ, 702, 1367
Brenneman, L. W., Reynolds, C. S., Nowak, M. A., et al. 2011, ApJ, 736, 103
Brightman, M., & Nandra, K. 2011, MNRAS, 413, 1206
Brinkmann, W., Otani, C., Wagner, S. J., & Siebert, J. 1998, A&A, 330, 67
Chiang, C.-Y., & Fabian, A. C. 2011, MNRAS, 414, 2345
Corbin, M. R. 1997, ApJS, 113, 245
Dadina, M. 2007, A&A, 461, 1209
Dauser, T., García, J., Parker, M. L., Fabian, A. C., & Wilms, J. 2014, MNRAS, 444, L100
de la Calle Pérez, I., Longinotti, A. L., Guainazzi, M., et al. 2010, A&A, 524, A50
Di Gesu, L., & Costantini, E. 2016, A&A, 594, A88
Fabian, A. C., Rees, M. J., Stella, L., & White, N. E. 1989, MNRAS, 238, 729
Fukazawa, Y., Hiragi, K., Mizuno, M., et al. 2011, ApJ, 727, 19
García, J., Dauser, T., Lohfink, A., et al. 2014, ApJ, 782, 76
George, I. M., & Fabian, A. C. 1991, MNRAS, 249, 352
Gofford, J., Reeves, J. N., Tombesi, F., et al. 2013, MNRAS, 430, 60
Gonzalez, A. G., Wilkins, D. R., & Gallo, L. C. 2017, MNRAS, 472, 1932
Graham, A. W. 2016, in Galaxy Bulges and Their Massive Black Holes: A Review, Astrophysics and Space Science Library, Vol. 418, ed. E. Laurikainen, R. Peletier, & D. Gadotti (Cham: Springer), 263
Guainazzi, M., Bianchi, S., & Dovčiak, M. 2006, AN, 327, 1032
Harrison, F. A., Craig, W. W., Christensen, F. E., et al. 2013, ApJ, 770, 103
Hasenkopf, C. A., Sambruna, R. M., & Eracleous, M. 2002, ApJ, 575, 127
Ikeda, S., Awaki, H., & Terashima, Y. 2009, ApJ, 692, 608
Jiménez-Bailón, E., Piconcelli, E., Guainazzi, M., et al. 2005, A&A, 435, 449
Kalberla, P. M. W., Burton, W. B., Hartmann, D., et al. 2005, A&A, 440, 775
Koyama, K., Tsunemi, H., Dotani, T., et al. 2007, PASJ, 59, 23
LaMassa, S. M., Cales, S., Moran, E. C., et al. 2015, ApJ, 800, 144
LaMassa, S. M., Yaqoob, T., Ptak, A. F., et al. 2014, ApJ, 787, 61
Larsson, J., Fabian, A. C., Ballantyne, D. R., & Miniutti, G. 2008, MNRAS, 388, 1037
Liu, Y., & Li, X. 2014, ApJ, 787, 52
Liu, Z., Yuan, W., Lu, Y., & Zhou, X. 2015, MNRAS, 447, 517
Lohfink, A. M., Fabian, A. C., Ballantyne, D. R., et al. 2017, ApJ, 841, 80
Lohfink, A. M., Reynolds, C. S., Miller, J. M., et al. 2012, ApJ, 758, 67
Madsen, K. K., Beardmore, A. P., Forster, K., et al. 2017, AJ, 153, 2
Mantovani, G., Nandra, K., & Ponti, G. 2016, MNRAS, 458, 4198
Middleton, M. 2016, in Astrophysics of Black Holes, Astrophysics and Space Science Library, Vol. 440, ed. C. Bambi (Berlin: Springer), 99
Miller, J. M. 2007, ARA&A, 45, 441
Mitsuda, K., Bautz, M., Inoue, H., et al. 2007, PASJ, 59, S1
Murphy, K. D., & Nowak, M. A. 2014, ApJ, 797, 12
Murphy, K. D., & Yaqoob, T. 2009, MNRAS, 397, 1549
Nandra, K. 2006, MNRAS, 368, L62
Nandra, K., O'Neill, P. M., George, I. M., & Reeves, J. N. 2007, MNRAS, 382, 194
Netzer, H., Maoz, D., Laor, A., et al. 1990, ApJ, 353, 108
Noda, H., Makishima, K., Nakazawa, K., et al. 2013, PASJ, 65, 4
Patrick, A. R., Reeves, J. N., Lobban, A. P., Porquet, D., & Markowitz, A. G. 2011, MNRAS, 416, 2725
Patrick, A. R., Reeves, J. N., Porquet, D., et al. 2012, MNRAS, 426, 2522
Pearson, T. J., Blundell, K. M., Riley, J. M., & Warner, P. J. 1992, MNRAS, 259, 13P
Peterson, B. M., Ferrarese, L., Gilbert, K. M., et al. 2004, ApJ, 613, 682
Porquet, D., Reeves, J. N., O'Brien, P., & Brinkmann, W. 2004, A&A, 422, 85
Reeves, J. N., & Turner, M. J. L. 2000, MNRAS, 316, 234
Reynolds, C. S. 2016, AN, 337, 404
Reynolds, C. S., Brenneman, L. W., Lohfink, A. M., et al. 2012, ApJ, 755, 88
Reynolds, C. S., & Nowak, M. A. 2003, PhR, 377, 389
Ricci, C., Ueda, Y., Paltani, S., et al. 2014, MNRAS, 441, 3622
Riley, J. M., & Warner, P. J. 1990, MNRAS, 246, 1P
Riley, J. M., Warner, P. J., Rawlings, S., et al. 1989, MNRAS, 236, 13P
Robinson, A., Corbett, E. A., Axon, D. J., & Young, S. 1999, MNRAS, 305, 97
Ross, R. R., Fabian, A. C., & Young, A. J. 1999, MNRAS, 306, 461
Sambruna, R. M., Eracleous, M., & Mushotzky, R. F. 1999, ApJ, 526, 60
Shu, X. W., Yaqoob, T., & Wang, J. X. 2010, ApJS, 187, 581
Shu, X. W., Yaqoob, T., & Wang, J. X. 2011, ApJ, 738, 147
Takahashi, T., Abe, K., Endo, M., et al. 2007, PASJ, 59, 35
Tombesi, F., Tazaki, F., Mushotzky, R. F., et al. 2014, MNRAS, 443, 2154
Tsujimoto, M., Guainazzi, M., Plucinsky, P. P., et al. 2011, A&A, 525, A25
Urry, C. M., & Padovani, P. 1995, PASP, 107, 803
Verner, D. A., Ferland, G. J., Korista, K. T., & Yakovlev, D. G. 1996, ApJ, 465, 487
Wilkins, D. R., & Fabian, A. C. 2011, MNRAS, 414, 1269
Wilkins, D. R., & Fabian, A. C. 2012, MNRAS, 424, 1284
Woo, J.-H., & Urry, C. M. 2002, ApJ, 579, 530
Yaqoob, T. 2012, MNRAS, 423, 3360
Yaqoob, T., George, I. M., Kallman, T. R., et al. 2003, ApJ, 596, 85
Yaqoob, T., & Murphy, K. D. 2011, MNRAS, 412, 277
Yaqoob, T., & Padmanabhan, U. 2004, ApJ, 604, 63
Yaqoob, T., Tatum, M. M., Scholtes, A., Gottlieb, A., & Turner, T. J. 2015, MNRAS, 454, 973
Yaqoob, T., Turner, T. J., Tatum, M. M., Trevor, M., & Scholtes, A. 2016, MNRAS, 462, 4038